6 August 2026

Infrasound waveguides on Venus could enable the detection of explosive volcanism using balloons

Sophus Bredesen Gullbekk[1,2], Quentin Brissaud[1], Marouchka Froment[1], Maxence Lefevre[3], Alexandra Michelle Iezzi[4], Sven Peter Näsholm[1,2]

1. NORSAR
2. Department of Informatics, University of Oslo
3. Sorbonne Universite
4. U.S. Geological Survey

Abstract

The prevalence of explosive volcanism on Venus is poorly constrained due to a lack of in-situ and remote sensing data. Balloon-borne pressure sensors in the middle atmosphere have the potential to detect infrasound from eruptions and thereby probe volcanic activity. In the current work, infrasound propagation is modeled using global wind and temperature fields from the Venus Climate Database, combined with an extension to the ray-based tau-p approach, as well as transmission loss simulations. We discover that strong zonal superrotation and subsolar-to-antisolar circulation generate persistent acoustic waveguides capable of channeling atmospheric infrasound in both zonal and meridional directions. To assess volcanic detectability, we couple global transmission loss estimates to a source model, relating Volcanic Explosivity Index to erupted mass, mass-flux histories, source pressure spectra, and Venus eruption statistics. Our statistical framework produces probability estimates of detecting at least one volcano for any target Signal-to-Noise Ratio for different balloon trajectories and mission durations. The results indicate that, for realistic noise levels, 6-month long balloon missions at ~60 km altitude can achieve up to 80% detection probability if only high-altitude volcanoes are considered. The detection rate varies with eruption duration, which drives the eruption pressure in our model. When considering long-duration eruptions, the detection probability drops below 30%, but it can reach 99% if all large volcanoes are considered active. The findings demonstrate that future long-duration balloon missions equipped with infrasound pressure sensors have great potential to provide novel data to constrain the rate and spatial distribution of explosive volcanism on Venus.

Posted on 6 August 2026 — The copyright holder is the author/funder. All rights reserved. No reuse without permission. — This is a preprint and has not been peer reviewed. Data may be preliminary. — https://doi.org/10.22541/essoar.15007111/v1

Keywords

Venus, Volcanoes, Infrasound, Balloons, Waveguides, Detectability

Posted on 6 August 2026 — The copyright holder is the author/funder. All rights reserved. No reuse without permission. — This is a preprint and has not been peer reviewed. Data may be preliminary. — https://doi.org/10.22541/essoar.15007111/v1

Infrasound waveguides on Venus could enable the detection of explosive volcanism using balloons

Sophus Bredesen Gullbekk [https://orcid.org/0009-0009-4250-6898][*1,2], Quentin Brissaud [https://orcid.org/0000-0001-8189-4699][*2], Marouchka Froment [https://orcid.org/0000-0002-2980-8711][2], Maxence Lefèvre [https://orcid.org/0000-0002-3143-9716][3], Alexandra M. Iezzi [https://orcid.org/0000-0002-6782-7681][4], and Sven Peter Näsholm [https://orcid.org/0000-0001-9107-4002][1,2]

[1]Department of Informatics, University of Oslo, Gaustadalléen 23B, 0373 Oslo, Norway
[2]NORSAR, Gunnar Randers vei 15, Kjeller, Norway
[3]LATMOS/IPSL, Sorbonne Université, UVSQ, Université Paris-Saclay, Centre National de la Recherche Scientifique, Paris, France
[4]U.S. Geological Survey, Volcano Science Center, Cascades Volcano Observatory, Vancouver, WA, USA

Abstract.

The prevalence of explosive volcanism on Venus is poorly constrained due to a lack of in-situ and remote sensing data. Balloon-borne pressure sensors in the middle atmosphere have the potential to detect infrasound from eruptions and thereby probe volcanic activity. In the current work, infrasound propagation is modeled using global wind and temperature fields from the Venus Climate Database, combined with an extension to the ray-based tau-p approach, as well as transmission loss simulations. We discover that strong zonal superrotation and subsolar-to-antisolar circulation generate persistent acoustic waveguides capable of channeling atmospheric infrasound in both zonal and meridional directions. To assess volcanic detectability, we couple global transmission loss estimates to a source model, relating Volcanic Explosivity Index to erupted mass, mass-flux histories, source pressure spectra, and Venus eruption statistics. Our statistical framework produces probability estimates of detecting at least one volcano for any target Signal-to-Noise Ratio for different balloon trajectories and mission durations. The results indicate that, for realistic noise levels, 6-month long balloon missions at ∼60 km altitude can achieve up to 80% detection probability if only high-altitude volcanoes are considered. The detection rate varies with eruption duration, which drives the eruption pressure in our model. When considering long-duration eruptions, the detection probability drops below 30%, but it can reach 99% if all large volcanoes are considered active. The findings demonstrate that future long-duration balloon missions equipped with infrasound pressure sensors have great potential to provide novel data to constrain the rate and spatial distribution of explosive volcanism on Venus.

Plain Language Summary. We explore whether pressure sensors carried by high-altitude balloons are likely to record volcanic eruptions on Venus. Using an established model of Venus's winds and temperatures, we simulate how low-frequency sound travels over long ranges from the surface and up to 60 km altitude. We discover that the strong winds in the atmosphere of Venus can trap the sound waves between specific altitudes, making it possible to propagate over long distances. We link this new knowledge with models for explosive volcanism on Venus and combine this with statistical estimates of how often and where eruptions might occur. This enables us to estimate the detection probabilities for different balloon flight paths and mission lengths. For realistic noise levels and different volcanic subsets, we find that long-duration balloon flights are likely to detect at least one explosive eruption during a mission. The findings show that future long-lasting Venus balloon missions carrying infrasound pressure sensors could provide new data that expand our knowledge about explosive volcanic activity on Venus.

Key Points

- We identify high-altitude waveguides on Venus that allow long-range broadband infrasound propagation from surface sources
- We develop a probabilistic framework to assess balloon detection of explosive infrasound for subsets of active volcanoes with an Earth-scaled eruption magnitude

*Corresponding author: Sophus Bredesen Gullbekk (sophus.gullbekk@norsar.no)

– Under the assumption of isotropic mass-driven sources, long duration balloon missions could likely detect highly impulsive explosive volcanism on Venus

1 Introduction

This work models the long-range propagation of low-frequency sound waves—infrasound—through the atmosphere of Venus. On Earth, ground-based infrasound is used to remotely monitor explosive events, including volcanic eruptions (e.g., *Gheri et al.*, 2025; *Perttu et al.*, 2020; *Dabrowa et al.*, 2011). But on Venus, the hostile surface environment prevents infrasound instrumentation, motivating the use of atmospheric balloons. For balloon-borne monitoring of Venus volcanism to be effective, the atmospheric conditions must be such that the sound waves are refracted back towards the balloons instead of dispersed into the upper atmosphere – forming natural acoustic *waveguides* – allowing the sound to reach distant balloon sensors.

Radar-based observation of Venus – one of the few techniques capable of imaging what lies beneath its thick aerosol clouds – has revealed a surface predominantly shaped by volcanism. Venus exhibits more than 100 large and about 80000 smaller-scale shield volcanoes (*Hahn and Byrne*, 2023), as well as lava flows, lava plains, and lava channels at a variety of scales (see, e.g., *Filiberto et al.*, 2025). Assessing the current level of volcanic activity on Venus remains a key to understanding its evolution and current geodynamic regime. Recent analyses of radar imagery from the Magellan mission have provided compelling evidence for ongoing volcanic activity, with surface changes observed on the north flank of Maat Mons (*Herrick and Hensley*, 2023), the western flank of Sif Mons and Niobe Planitia (*Sulcanese et al.*, 2024) occurring between 1990 and 1992. These surface changes are consistent with the deformation of eruptive vents and fresh lava flows.

The morphology of Venus's volcanoes and lava flows, and their resemblance with Earth's shield volcanoes suggests a dominance of effusive eruptions, producing a basaltic magma. Signs of eruptions of Plinian, Strombolian or Vulcanian types, which feature transient or continuous explosive activity and plumes, are comparatively rare on the surface. Still, there are radar observations suggesting the presence of pyroclastic deposits in proximity of volcanic provinces that would support the existence of explosive eruptions: in Dione Regio (*Keddie and Head*, 1995; *Campbell et al.*, 2017; *Ganesh et al.*, 2022), Guinevre Planitia (*Head et al.*, 1991), Eistla Regio (*Campbell et al.*, 2017; *Ganesh et al.*, 2022), Phoebe Regio (*Campbell et al.*, 2017), and the unique Scathas Fluctus (*Ghail et al.*, 2024). Domes with steep sides, analogous to dacite-rhyolite domes on Earth, are also found in Alpha regio, and could host occasional explosive activity as gases break through (*Head et al.*, 1991). The limited resolution of current radar data and its lack of polarization data (which provides information on surface roughness) mean that many similar features could be missed, and pyroclastic flows could be more widespread (*Filiberto et al.*, 2025).

The rarity of these explosive eruption regimes can be explained by a combination of a low volatile content in the magma, which could limit the exsolution of gases and the formation of bubbles, and the high surface temperature and pressure conditions on Venus (more than 700 K and 90 bars at ground level), which prevent the fast expansion of gases and lead to early plume collapse. Eruptive column modeling studies show that an abnormally high volatile content (2.5 to 5 wt% (*Garvin et al.*, 1982; *Head and Wilson*, 1986)) would be needed to achieve the volume fraction of bubbles necessary for lava fragmentation and explosion. However, if Plinian-type eruptions are unlikely, occasional Vulcanian or Strombolian eruptions could occur (*Fagents and Wilson*, 1995). *Airey et al.* (2015) showed that the requirements for volatile content decrease as the elevation of the volcano increases, due to the lower atmospheric pressure. Hence, only ~ 2 wt% H_2O would be needed to produce fragmentation at Maat Mons, and a concentration of 4.7 to 6 wt% of mixed H_2O or CO_2 could enable the formation of ~ 20 km high plumes. *Lefèvre et al.* (2025) conducted a sensitivity study of plume vertical propagation using an eruption column model in a realistic Venusian atmosphere, and reached similar conclusions, finding that pseudo-stable plumes are possible and more likely at high elevation and high latitudes. On Earth, submarine volcanoes erupt under similar high-pressure conditions but the largest are nevertheless capable of producing explosive activity and plumes that breach the water surface (*Clague et al.*, 2009; *Resing et al.*, 2011; *Helo et al.*, 2011).

Despite this modeling-based evidence, the exact composition in volatiles of the Venus magma is largely unknown. In addition, CO_2 in the lower atmosphere of Venus is in a supercritical state, with properties between a gas and a liquid leading to altered solubility and compressibility (*Averbuch et al.*, 2023). The ways in which this state could affect eruption dynamics have not yet been thoroughly investigated. Producing convincing evidence for explosive volcanism and plume formation on Venus thus requires novel and direct observations. The limited temporal coverage and spatial resolution of radar observations, combined with the thick cloud layer of Venus, hinder the ability of remote sensing to capture transient phenomena, such as explosions and plume collapses. However, a window of opportunity lies in the fact that volcanic explosions and plumes emit infrasound waves that may propagate efficiently through the dense atmosphere of Venus. Even in the absence of large plumes, bubble bursts and dome-collapse events associated with effusive volcanism can generate strong acoustic and infrasonic signals, as demonstrated by terrestrial analogs such as Strombolian eruptions and submarine bubble bursts (see, e.g., *Vergniolle et al.*, 1996; *Resing et al.*, 2011; *Fee and Matoza*, 2013; *Crone and Bohnenstiehl*, 2019). Thus, even moderate effusive eruptions on Venus may act as detectable infrasound sources – but only under the condition that the atmosphere structures would enable the sound to be ducted through waveguides from the source to a receiving acoustic sensor.

Byrne and Krishnamoorthy (2022) used a simple scaling to compare terrestrial and Venusian eruption dynamics, highlighting that eruptions with a Volcanic Explosivity Index (VEI) greater than zero are likely to occur within any 60-day observation window. This timescale is particularly relevant to proposed Venus balloon missions, which are expected to remain aloft for several months (*Garcia et al.*, 2024; *Cutts et al.*, 2025). Balloons equipped with high-sensitivity pressure sensors might hence be able to detect infrasonic signatures of volcanic activity, offering a novel means of constraining eruption rates and spatial distributions.

Recent studies have estimated the detectability of atmospheric sound waves produced by seismo-acoustically coupled venusquake-generated seismic surface waves (*Brissaud et al.*, 2026; *Garcia et al.*, 2024). When estimating the likelihood of detecting these sounds in data recorded by balloon-borne acoustic sensors and satellite-borne airglow cameras, it was found with high confidence that venusquakes will be detected for missions longer than 6 months (*Brissaud et al.*, 2026). Independent of the source mechanism, an estimate of the background acoustic noise level is needed to estimate the detectability of acoustic signals. As the noise level experienced by balloons on Venus is not well-constrained, we assume it to be on the same order of magnitude as on Earth ($\sim 10^{-2}$ Pa) (*Brissaud et al.*, 2026; *Garcia et al.*, 2024).

Compared to sound generated from seismo-acoustic venusquakes, volcanic eruptions are of particular interest, because they are typically radiated in all directions, and not only vertically. Therefore, these waves have the potential to insonify the atmosphere over much longer ranges.

Compared to the current study that analyzes long-range propagation of infrasound from volcanoes, previous works on acoustic propagation in Venus's atmosphere are limited in scope: For example, the venusquake detectability study of *Garcia et al.* (2024) looked at sound from seismic surface-wave sources under the assumption that these only generate vertically propagating sound that is neither refracted, nor ducted over long ranges in Venus's atmosphere. The only detailed infrasound propagation modeling study published to date, by *Averbuch et al.* (2023), focused on altitudes below 20 km, which is below the heights relevant for balloon observations ($\sim$60 km), and which cannot capture the long-range ducting considered in the current study. The recent detectability assessments of *Brissaud et al.* (2026) are based on empirical propagation models and predicted at least three volcanic detections per 60-day mission. However, these results relied on oversimplified propagation schemes that neglect the influence of detailed models of Venus atmospheric wind and temperature profiles, as well as the associated long-range wave ducting.

The trajectory of atmospheric infrasound waves is governed by refraction, which can be described by the effective sound speed $c_{\text{eff}} = c + \mathbf{w}$, where c is the adiabatic sound speed and $\mathbf{w}$ is the projected wind in the direction of propagation. Following Snell's law, acoustic waveguides are formed due to the presence of gradients in the effective sound speed that cause them to bend and refract towards altitudes with lower effective sound speed. In some cases, the waves become trapped between two altitudes; forming a waveguide. These guided waves experience less decay and can therefore propagate over much larger distances. As an example, the SOund Fixing And Ranging (SOFAR) channel at around 1 km depth in the ocean, and the atmoSOFAR channel in the stratosphere (*Albert et al.*, 2023), are known to efficiently duct sound waves over long ranges on Earth.

In contrast to Earth, Venus's temperature decreases steeply with altitude and since the adiabatic sound speed is proportional to the square root of temperature, there is no temperature-driven positive gradient in sound speed to produce the refraction patterns required for the formation of long-range, upper-atmospheric waveguides. Therefore, if such waveguides exist, they are likely wind-driven, but this possibility has not yet been investigated in detail, and the associated research question is open.

There are two main wind regimes on Venus that could facilitate long range infrasound propagation through elevated waveguides (see *Schubert et al.*, 2007, for an overview). From the ground to $\sim$70 km altitude, a Retrograde Super-rotational (RSR) wind dominates – circling from east to west faster than the planet's self rotation – with wind speeds exceeding 100 m/s at the cloud tops (Fig. 1c) (*Sánchez-Lavega et al.*, 2017; *Horinouchi et al.*, 2024). Further up, the winds become strongly dependent on the Sun's position in the sky (*Navarro et al.*, 2021). Exposed regions heat up, creating strong Subsolar-to-Antisolar (SS-AS) winds that flow from the day-side to the night-side of the planet (Fig. 1d). Although the atmosphere shows limited seasonal variations, winds may vary with altitude, location, and local true solar time (see Fig. 1(c,d)), keeping in mind that a Venus day corresponds to around 117 Earth days. Wind fluctuations near topographic features and transitions between day and night sides can alter local temperature and stability profiles, potentially generating acoustic waveguides. The existence, structure, and variability of these waveguides remain poorly understood, which severely limits our ability to assess the detectability of explosive events using acoustic data recorded at balloon platforms. A more complete understanding of infrasound propagation in Venus's atmosphere is therefore essential to evaluate the feasibility of volcanic detection from future missions that include aerial platforms with acoustic sensors.

In the current study, we investigate the ducting of volcanic infrasound to balloon platforms in the Venusian atmosphere. Using realistic atmospheric conditions provided by planetary climate models and volcanic source property estimates, we assess the expected signal amplitudes at balloon altitudes and quantify the likelihood of event detection by pressure sensors carried by these platforms. Under realistic background acoustic noise level assumptions, our results provide new constraints on both the detectability of volcanic activity and the diagnostic potential of infrasound observations for ongoing geophysical processes on Venus. This global propagation modeling morphology is coupled to a VEI-based volcanic source model and a Poisson-distribution based eruption framework, linking erupted mass and mass-flux histories to peak source pressure, in order to estimate signal-to-noise–based detection probabilities for different balloon trajectories and mission durations.

2 Methodology

In this section, we describe the numerical modeling approaches adopted to determine the presence of infrasound wave ducting on Venus from omnidirectional sources close to the surface (such as events related to explosive volcanism) to balloons placed in the middle atmosphere.

Geometrical spreading, wave ducting, and intrinsic attenuation losses all contribute to the amplitude reduction of a sound wave as it propagates from source to receiver. This reduction, relative to a unit amplitude source, is commonly referred to as the Transmission Loss (TL). To explore the global infrasound ducting morphology on Venus, we combine two approaches: 1) we identify ducting using an extension of the ray-theory-based tau-p approach that describes how infinite frequency rays would refract through the atmosphere; and 2) we simulate TL using a parabolic-equation solver that provides a more accurate description of the low-frequency wavefield. Both approaches require a model of atmospheric conditions as a function of space and time on Venus.

While the tau-p based approach used is computationally efficient, it is limited to range-independent atmospheric conditions, and relies on ray theory, which assumes that sound waves have an infinite frequency (*Garcés et al.*, 1998). The parabolic equation offers another formulation of the equations of sound propagation, which accounts for diffraction effects observed at low frequencies (*Waxler and Assink*, 2018). It can handle range-dependent atmospheric specifications but is associated with a significantly greater computational burden, although it is worth mentioning that machine-learning based approaches have been shown potential to drastically speed up these calculations (*Brissaud et al.*, 2023; *Cameijo et al.*, 2025).

Finally, we describe a probabilistic framework, which combines infrasound amplitude information with a model for volcanic source pressure, to yield a statistical estimate of the detectability of Venus volcanism from a balloon platform.

2.1 Atmospheric temperature, wind, and attenuation specifications

Wind and sound speed profiles of Venus's atmosphere are extracted from the Venus Climate Database (VCD) version 2.3 (*Lebonnois et al.*, 2010, 2016; *Martinez et al.*, 2023). The VCD framework calculates the sound speed as $c = \sqrt{\gamma P/\rho}$, using the local atmospheric pressure P, density ρ, and ratio of specific heats γ. The VCD can provide output for different cloud albedo and Extreme Ultraviolet (EUV) scenarios. The EUV radiation affects the temperature in the upper atmopshere, while the cloud albedo determines the fraction of solar radiation reflected by the dense clouds in the middle atmosphere. This study uses the average EUV and standard cloud albedo scenario of the VCD. VCD profiles span altitudes from 0 to 157 km, where 0 km corresponds to the mean radius of the planet. In regions of elevated topography, profiles are linearly extrapolated down to the mean radius, producing a flat representation of the planet that is suitable for our modeling.

To simulate infrasound propagation and analyze the prospects of long-range wave ducting, a range-dependent atmospheric representation is required. To this end, vertical profiles are sampled every 300 km along geodesic lines and combined into 2D vertical slices. The horizontal resolution is chosen as a compromise between computational efficiency and the native resolution of the VCD (1.875° in latitude and 3.75° in longitude). Each range-dependent slice is extracted at a fixed Universal Solar Time (UST), thus providing variation in local true solar time at different longitudes relative to longitude 0. This is done to capture the large variations in upper atmospheric SS-AS winds along the twilight zones, where the propagation conditions might vary substantially along a single profile (see Fig. 1(d)). The profiles in the VCD include high Mach number thermospheric winds along the solar terminators (*Navarro et al.*, 2021). In headwind conditions, these winds are tapered to zero, causing the waves to dissipate into the upper atmosphere, as these winds can generate sound waves with a considerable backwards component.

A realistic attenuation model is required to quantify the intrinsic energy loss of infrasound during propagation. In the frequency range of interest, this loss is mainly governed by CO_2 relaxation (see *Petculescu*, 2016; *Garcia et al.*, 2017, 2024, for further details). Additional acoustic attenuation may also arise in the global cloud layer (45–70 km altitude) from sulfuric acid droplet dynamics (*Trahan and Petculescu*, 2020) and high-altitude molecular diffusion (*Piñeyro et al.*, 2026).

In the current work, we apply the intrinsic attenuation model from (*Garcia et al.*, 2024). Fig. 1(a, b) compares the attenuation in this Venus model to the Sutherland-Bass model for Earth (*Sutherland and Bass*, 2004). The cumulative attenuation in Fig. 1(b) represents the total loss experienced by a wave as it propagates from the surface to a given altitude. We highlight that infrasound attenuation on Venus is generally lower than on Earth, favoring long-range propagation of infrasound, except within the dense cloud layer, where the intrinsic attenuation models are comparable. In the current work, we disregard any effects related to non-linear wave propagation (*Hamilton and Blackstock*, 1998).

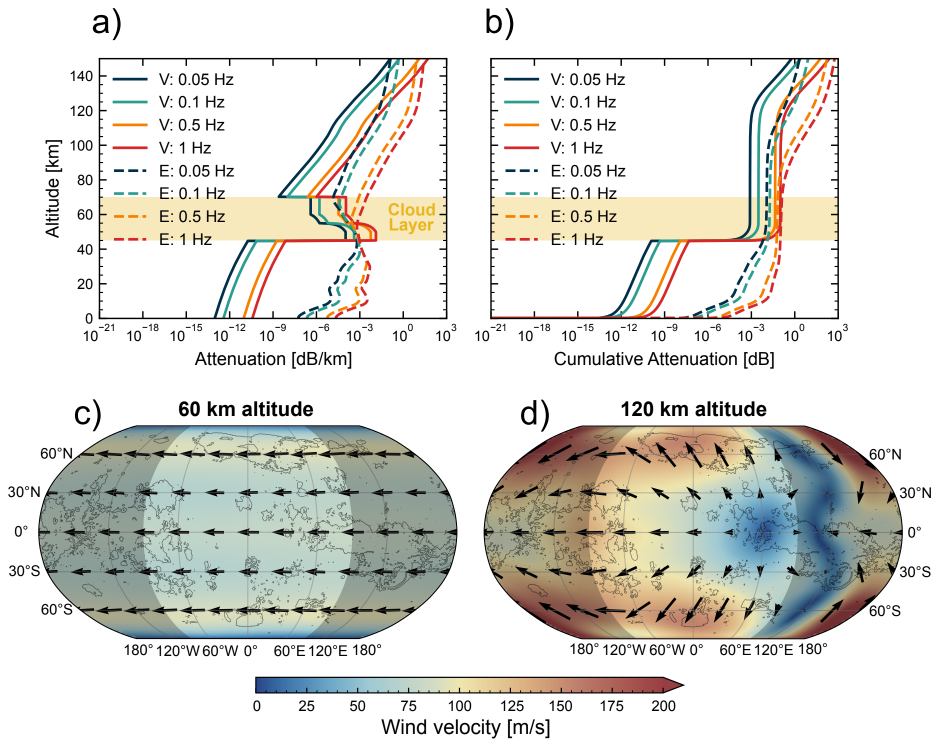

Figure 1. The attenuation profiles **(a)** in dB/km used on Venus (Same as Fig. 1. in *Garcia et al.*, 2024) (V, solid lines) compared to the Sutherland-Bass model for Earth (E, dashed lines) using four different frequencies. In **(b)**, the corresponding cumulative attenuation is shown i.e. the total loss a plane wave would experience from the ground to each altitude. The yellow highlights indicate altitudes covered by clouds. The second row shows a snapshot of the Venusian atmosphere at 12:00 UST. The RSR winds at 60 km altitude is shown in **(c)**, and the SS-AS winds at 120 km altitude is shown in **(d)**. The arrows indicate the direction and speed of the winds and shaded regions represents areas in shadow. All altitudes are relative to the mean radius of Venus.

2.2 Assessing the presence of waveguides using ray-theoretic and parabolic-equation based approaches

2.2.1 Extending the tau-p method to find elevated waveguides

The effective sound speed approximation is applied for all propagation analyses. In this approach, instead of modeling wave propagation in a moving-medium model, an effective motionless medium is defined (*Godin*, 2002). Here, the projection of the wind in the horizontal propagation direction is added to the background sound speed which greatly simplifies the propagation simulation. This approach is valid for shallow vertical propagation angles and sufficiently low Mach numbers for the wind speed. The effective sound speed approximation is commonly applied in infrasound studies, although it can to some extent influence modeled travel times, direction of arrival, and absorption (*Assink et al.*, 2017).

The tau-p method is a ray-theory founded framework previously used to identify ground-to-ground waveguides on Earth (*Drob et al.*, 2003, 2010; *Garcés et al.*, 1998). In *Drob et al.* (2003, 2010), the vertical ray slowness $q_r(z)$ is used to find the turning points of individual rays $r(\theta, \phi)$, each defined by a launch azimuth θ and inclination ϕ. The turning points occur where the vertical ray component vanishes, which corresponds to $q_r(z) = 0$ (See *Drob et al.*, 2010, Eq. 1–4 for more details).

Here, the we extend the ground-to-ground tau-p method to take into account waveguides relevant for propagation from close to ground to sensor platforms at altitude. This requires searching for the roots of $q_r(z)$ that correspond to altitudes above $A(r)$ and below $B(r)$. Looking at these as a function of balloon altitude z_b, we seek to find the conditions that fulfill:

$$A(r) = \min\{z > z_b \,|\, q_r(p, z) = 0\} \quad \text{and} \quad B(r) = \min\{z < z_b \,|\, q_r(p, z) = 0\}. \tag{1}$$

To account for any propagation direction, the θ and ϕ values are sampled uniformly from a tessellated sphere using the `stripy` Python library (*Moresi and Mather*, 2019). The rays are launched reciprocally from balloon locations at 60 km altitude, effectively switching the role of source and receiver according to the reciprocity principle and the flow-reversal theorem, as further described below. This is done to facilitate the inclusion of sources with varying vertical distributions, such as volcanic plumes, while maintaining computational efficiency. Based on the turning heights given by solutions to Eq. 1, the rays can be grouped into three different categories: Ground rays, trapped rays, and escaped rays. To quantify how many rays fall in each category, we calculate their ducting fractions, i.e., the amount of rays in each category divided by the total number of rays. Of particular interest are the trapped ducting fractions (see Supplementary Sec. S2), as high values indicate elevated waveguides capable of long-range ducting of infrasound at balloon altitudes.

The reciprocity principle in linear wave propagation states that in a given isotropic medium, exchanging the source and receiver positions will yield the same Green's function solution to the wave equation (see, e.g., *Carcione*, 2007, Chapter 5 for a historical overview). However, for a moving medium, such as an ocean with currents or a windy atmosphere, the current or wind components also have to be reversed for reciprocity to hold. This extension of the principle is denoted the flow-reversal theorem. We refer the reader to *Godin* (1997); *Lalande et al.* (2012) for further explanations and an example of application of this principle to infrasonic wave propagation. In the current study, this implies that, as an alternative to launching many simulations that model infrasound ray paths from many source locations to a given receiver location, we can instead find the same ray paths by applying the reciprocity principle (with reversed wind components according to the flow-reversal theorem) using a single simulation run, with the receiver location used as the source location.

2.2.2 Parabolic-equation based TL estimation and waveguide assessment

While the geometric tau-p approach enables us to quickly explore a range of atmospheric parameters, ducting properties, and source and observation locations, it does not account for frequency dependent ducting nor amplitudes. Therefore, to better capture frequency-dependent path effects, we ran TL simulations from a surface source towards various azimuths. The reported TL is the attenuation of the wave in dB, which is given by the pressure P at a receiver location relative to the pressure 1 km from the source:

$$\mathrm{TL}(r,z) = 20\log_{10}\left(\frac{|P(r,z)|}{|P_0|}\right), \tag{2}$$

where P_0 is the reference pressure at a distance of 1 km from the source, while r and z represent the horizontal range and altitude relative to the source, respectively.

To perform the TL simulations, the finite-frequency software ePape from the NCPAprop code package (*Waxler et al.*, 2021; *Waxler and Assink*, 2018; *Waxler et al.*, 2022) is used to model the wavefield evolution in terms of a frequency-dependent TL. This parabolic equation-based solver allows us to compute range-dependent TL to estimate the detectability of explosive volcanic events. To model the global morphology of waveguides on Venus for elevated platforms, we sample locations on a 3.75°×3.75° grid. For each location, we simulate range-dependent atmospheric profiles along 12 evenly spaced azimuths. Each range-dependent slice has a maximum range of 3000 km to ensure a geometrical spreading error below 2.5%. Here again, the reciprocity principle and flow-reversal theorem are applied. For each resulting location–azimuth pair, the wave is launched from the balloon altitude (60 km, which is in the upper part of the cloud layer). The TL is recorded for source altitudes between 0 and 12 km above the mean radius of the planet. For illustration, Fig. S2.1(a,b) in Supplementary Sec. S2 compares the turning heights of a single trapped ray with the corresponding finite-frequency wavefield generated by an elevated source. Due to reciprocity, energy reaching the surface implies that volcanic eruptions can be detected at altitude. To enable the use of TL for global detectability, we extrapolated TL values, in db, beyond 3000 km from the source by performing a linear fit on the last 2000 km. This extrapolation assumes that the average db loss beyond 1000 km remains constant at a global scale.

2.3 Using TL estimates to get explosive volcanic event detection probability estimates

We want to determine the probability that at least one volcanic eruption generates infrasound signals exceeding a certain Signal-to-Noise Ratio (SNR). Assuming that the distribution of eruptions over a given time period follows a Poisson distribution at each volcano, this probability can be described as a Poisson process, such that:

$$\mathbb{P}(n_{\mathrm{detect}} \geq 1; \mathrm{SNR} \geq d, \sigma_n, \mathbf{x}^{\mathrm{obs}}, t) \quad = \quad 1 - \exp\left[-\lambda(\mathrm{SNR} > d; \sigma_n, \mathbf{x}^{\mathrm{obs}})t\right], \tag{3}$$

where $\mathbb{P}(n_{\mathrm{detect}} \geq 1; \mathrm{SNR} \geq d, \sigma_n, \mathbf{x}^{\mathrm{obs}}, t)$ is the probability of observing at least one eruption ($n_{\mathrm{detect}} \geq 1$) with a Signal-to-Noise Ratio $\mathrm{SNR} > d$ from a balloon location $\mathbf{x}^{\mathrm{obs}}$, with a balloon noise level σ_n (Pa), over a mission duration t (years), and where $\lambda(\mathrm{SNR} > d; \sigma_n, \mathbf{x}^{\mathrm{obs}})$ is the rate of eruptions producing signals with SNR exceeding d. The rate λ depends on the yearly rate of volcanic eruptions above a intensity $\mathrm{VEI}_{\mathrm{min}}$ at each volcano, expressed as $\lambda^{\mathrm{v}}(\mathrm{VEI} > \mathrm{VEI}_{\mathrm{min}})$, as well as on the probability of detecting eruptions from a specific volcano v from the balloon location $\mathbb{P}(\mathrm{SNR} > d|\mathrm{v})$, such that

$$\lambda(\mathrm{SNR} > d) = \sum_{\mathrm{v}} \lambda^{\mathrm{v}}(\mathrm{VEI} > \mathrm{VEI}_{\mathrm{min}})\mathbb{P}(\mathrm{SNR} > d|\mathrm{v}; \sigma_n, \mathbf{x}^{\mathrm{obs}}), \tag{4}$$

where $\mathrm{VEI}_{\mathrm{min}}$ is the minimum Volcanic Explosive Index considered. We extract estimates for the yearly rate of eruptions at each volcano λ^{v} from a recent Earth-to-Venus scaling study (*Byrne and Krishnamoorthy*, 2022). To build the yearly eruption rate (Fig. 2a), we multiply the probability of eruptions per VEI on Earth from the Global Volcanism Program (GVP) database for all volcano classes (Table 1 in *Byrne and Krishnamoorthy* (2022)) with the yearly number of new volcanic eruptions on Venus that last less than 100 days (Table S2 from *van Zelst* (2022) which corrects Table 4 from *Byrne and Krishnamoorthy* (2022)). The probability of detecting signals from a given volcano $\mathbb{P}(\mathrm{SNR} > d|\mathrm{v}; \sigma_n, \mathbf{x}^{\mathrm{obs}})$ is obtained by integrating the probability of detecting a specific event over the range of possible VEI, which reads

$$\mathbb{P}(\mathrm{SNR} > d|\mathrm{v}; \sigma_n, \mathbf{x}^{\mathrm{obs}}) = \int_{\mathrm{VEI}=\mathrm{VEI}_{\mathrm{min}}}^{\mathrm{VEI}_{\mathrm{max}}} \mathbb{P}(\mathrm{SNR} > d|\mathrm{VEI}, \mathbf{x}^{\mathrm{v}}; \sigma_n, \mathbf{x}^{\mathrm{obs}}) f^{\mathrm{v}}(\mathrm{VEI})\, d\mathrm{VEI}, \tag{5}$$

where $\mathbb{P}(\mathrm{SNR} > d|\mathrm{VEI}, \mathbf{x}^{\mathrm{v}}; \sigma_n, \mathbf{x}^{\mathrm{obs}})$ is the probability of detecting eruptions of a given VEI and from a distance r (km), and $f^{\mathrm{v}}(\mathrm{VEI})$ is the Probability Density Function (PDF) of an event with a specific VEI, that reads

$$f^{\mathrm{v}}(\mathrm{VEI}) \quad = \quad \mathbb{P}(\mathrm{VEI} \geq x \geq \mathrm{VEI}_{\mathrm{min}}) = -\frac{\partial}{\partial \mathrm{VEI}} \frac{\lambda^{\mathrm{v}}(\mathrm{VEI} \geq x \geq \mathrm{VEI}_{\mathrm{min}})}{\lambda^{\mathrm{v}}(x \geq \mathrm{VEI}_{\mathrm{min}})}, \tag{6}$$

Finally, the probability of detecting a specific event, from a given volcano at a location $\mathbf{x}^{\mathrm{v}}$, $\mathbb{P}(\mathrm{SNR} > d|\mathrm{VEI}, r)$ used in Eq. 5 corresponds to the probability of an eruption to produce a signal with $\mathrm{SNR} > d$ integrated over all possible SNR values above d such that

$$\mathbb{P}(\mathrm{SNR} > d|\mathrm{VEI}, \mathbf{x}^{\mathrm{v}}; \sigma_n, \mathbf{x}^{\mathrm{obs}}; f) = \int_{\mathrm{SNR}=d}^{\infty} f_{\mathcal{A}}(\mathrm{SNR}; \mathrm{VEI}, \mathbf{x}^{\mathrm{v}}, \sigma_n, \mathbf{x}^{\mathrm{obs}}, f)\, \mathrm{dSNR}, \tag{7}$$

where $f_{\mathcal{A}}(\mathrm{SNR} = d; \mathrm{VEI}, \mathbf{x}^{\mathrm{v}}, \sigma_n, \mathbf{x}^{\mathrm{obs}})$ is the PDF of a Gaussian distribution for a specific eruption to generate a signal with $\mathrm{SNR} = d$ defined as

$$\mathcal{A} \sim \mathcal{G}\left(\frac{\mathrm{A}(\mathrm{VEI}, \mathbf{x}^{\mathrm{v}}, \mathbf{x}^{\mathrm{obs}}, f)}{\sigma_n}, \sigma_{\mathrm{TL}}\right), \tag{8}$$

where σ_{TL} (dB) is the TL estimation uncertainty, that we set at an arbitrarily low value of 1% of the predicted TL, and A is the VEI-derived amplitude model A (Pa) that reads

$$\mathrm{A}(\mathrm{VEI}, \mathbf{x}^{\mathrm{v}}, f) = p_{R,\mathrm{peak}}(\mathrm{VEI}, f) 10^{\mathrm{TL}(\mathbf{x}^{\mathrm{v}}, \mathbf{x}^{\mathrm{obs}}, f)/20}, \tag{9}$$

where $p_{R,\mathrm{peak}}$ (Pa) is the peak pressure at a distance R (m) from the source, and TL (dB) stands for Transmission Loss from a that distance R, calculated using the parabolic equation method described in Section 2.2.2.

2.4 Relating VEI and source pressure

The amplitude model $\mathrm{A}(\mathrm{VEI}, \mathbf{x}^{\mathrm{v}}, f)$ requires to connect VEI to peak source pressure $p_{R,\mathrm{peak}}$. However, VEI is a qualitative measure of volume of erupted material and eruption duration (*Newhall and Self*, 1982), and it is challenging to relate it directly to pressure. Using Earth data, *Galetto et al.* (2023) investigated the empirical relationship between VEI and eruption magnitude M_g, where $\mathrm{M}_g = \log_{10} m - 4$ with m (kg) the erupted mass. The authors observed that eruption magnitudes follow a Gaussian distribution for VEI between 1 and 6 for explosive eruptions such that $\mathbb{P}(M_g|\mathrm{VEI}) = \mathcal{G}[\mu(\mathrm{VEI}), \sigma(\mathrm{VEI})]$, where μ and σ are the mean and standard deviation for each VEI. The advantage of using eruption magnitude is that it is solely defined in terms of erupted mass, which can be related to a monopole pressure source through the mass rate $\dot{m}(\mathrm{M}_g, t)$ (such that $m(\mathrm{M}_g) = \int_t \dot{m}(\mathrm{M}_g, t)\, dt$). Assuming that $\dot{m}$ follows a linear ramp from 0 to $\dot{m}_{\max}$, with a rise time τ_r (s), a fall time τ_f (s) and a eruption duration of high-intensity mass ejection from the volcano T_{dur}, the mass m reads

$$m(\mathrm{M}_g) \quad = \quad \dot{m}_{\max}(\mathrm{M}_g)(T_{\mathrm{dur}} + \frac{1}{2}(\tau_r + \tau_f)), \tag{10}$$

Here we will assume for simplicity $\tau_r = \tau_f$. Assuming a monopole source, the pressure at a reference distance R (m) can be approximated as

$$\tilde{p}_R(\mathrm{M}_g, t) = \frac{1}{4\pi R} \frac{\partial}{\partial t} \dot{m}(\mathrm{M}_g, t), \tag{11}$$

Peak acoustic pressure $\tilde{p}_{R,\mathrm{peak}}$ (Pa) is therefore connected to the maximum of the derivative of the mass rate $\max_t \frac{\partial}{\partial t} \dot{m}(\mathrm{M}_g, t)$. In a narrow frequency band around a frequency f, we can write $\tilde{p}_{R,\mathrm{peak}}(\mathrm{M}_g, f) \approx \mathcal{F}\left\{\frac{\partial}{\partial t}\dot{m}\right\}(\mathrm{M}_g, f)$, where $\mathcal{F}$ is the Fourier transform. We then approximate $\mathcal{F}\left\{\frac{\partial}{\partial t}\dot{m}\right\}$

with its upper envelope such that (see Supplementary Sec. S1)

$$\mathcal{F}\left\{\frac{\partial}{\partial t}\dot{m}\right\}(\mathrm{M}_g, f) \approx \dot{m}_{\max}(\mathrm{M}_g)\left[\frac{2}{\sqrt{1+\pi f \tau_r}}\right]. \tag{12}$$

Then we can relate the peak pressure to the eruption magnitude such that

$$\begin{aligned}
\tilde{p}_{R,\mathrm{peak}}(\mathrm{M}_g, f) &\approx \frac{1}{4\pi R}\mathcal{F}\left\{\frac{\partial}{\partial t}\dot{m}\right\}(\mathrm{M}_g, f) & (13)\\
&\approx \frac{\dot{m}_{\max}(\mathrm{M}_g)}{4\pi R}\left[\frac{2}{\sqrt{1+\pi f \tau_r}}\right],\\
&= \frac{1}{4\pi R}\frac{m(\mathrm{M}_g)}{T_{\mathrm{dur}}+\tau_r}\left[\frac{2}{\sqrt{1+\pi f \tau_r}}\right],\\
&= \frac{1}{4\pi R}\frac{10^{\mathrm{M}_g+4}}{T_{\mathrm{dur}}+\tau_r}\left[\frac{2}{\sqrt{1+\pi f \tau_r}}\right]. & (14)
\end{aligned}$$

Then the VEI-derived peak pressure $p_{R,\mathrm{peak}}(\mathrm{VEI}, f)$ can be expressed in terms of magnitude-derived peak pressure $\tilde{p}_{R,\mathrm{peak}}(M_g, f)$ as

$$p_{R,\mathrm{peak}}(\mathrm{VEI}, f) = \int_{\mathrm{M}_g=1}^{7} \mathbb{P}(M_g|\mathrm{VEI})\tilde{p}_{R,\mathrm{peak}}(M_g, f)\, d\mathrm{M}_g. \tag{15}$$

Variations in peak pressure $\tilde{p}_{R,\mathrm{peak}}$ are primarily driven by magnitude, while frequency has a minimal impact in the range of frequencies considered here (Fig. 2b). For $\mathrm{T}_{\mathrm{dur}} = 10$ s, peak pressure is between 1 to 10^6 Pa for the range of source parameters investigated, which is a reasonable range for magnitudes up to 6. Peak mass rates $\dot{m}_{\max}$, extracted from Eq. 10, show values between 10^4 to 10^{10} Pa up to magnitude 6 (Fig. 2c) which includes the range of mass rates, above 10^7 kg/s, investigated by *Lefèvre et al.* (2025) that trigger explosive volcanism with high-altitude plumes. We can also derive other source parameters from the peak mass rate, such as the exit velocity v_0 (m/s) as $v_0 = \dot{m}_{\max}/\pi\rho_{\mathrm{exit}}r^2$, where ρ_{exit} (kg/m^3) is the plume density and r (m) is the vent radius (*Lefèvre et al.*, 2025). Exit velocities, computed for $\rho_{\mathrm{exit}} = 200$ kg/m^3 and $r = 100$ m, show values between 10 and 10^3 m/s for an eruption magnitude 6 (Fig. 2d), which is close to the maximum exit velocity of 340 m/s investigated by *Lefèvre et al.* (2025). Note that decreasing the vent radius will significantly increase the exit velocity which would lead to unrealistic velocity values for large eruption magnitudes.

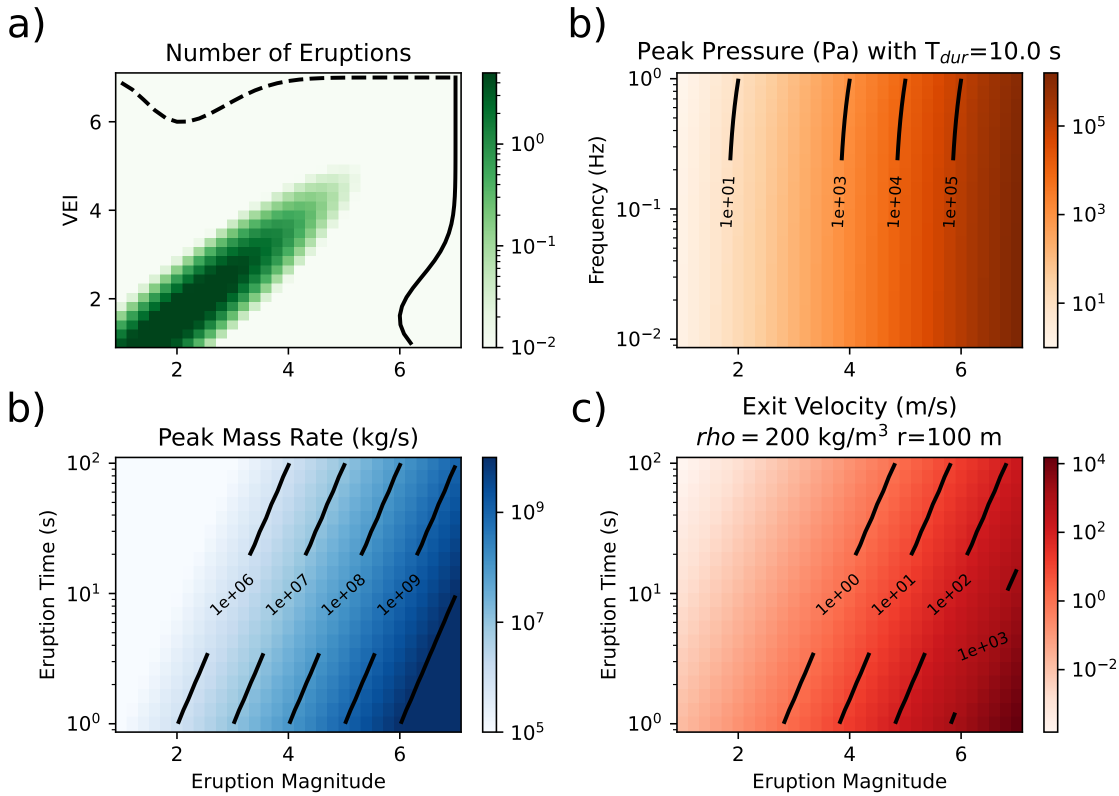

Figure 2. Volcanic source model. (a) Distribution of yearly number of eruptions vs eruption magnitude for each VEI. The black lines show the 1D distribution of events for each VEI (solid line) and for each magnitude (dashed line). (b) Magnitude-derived peak pressure $\tilde{p}_{R,\text{peak}}$, defined in Eq. 14, for an eruption time $\text{T}_{\text{dur}} = 10$ s and a rise time $\tau_r = 0.5$ s. (c) Peak mass rate (kg/s) $\dot{m}_{max}$ defined in Eq. 10 and (d) Exit Velocity (m/s), defined as $v_0 = \dot{m}_{\text{max}}/\pi\rho_{\text{exit}}r^2$ with the plume density $\rho_{\text{exit}} = 200$ kg/m^3 and vent radius $r = 100$ m, vs eruption magnitude and eruption time T_{dur} (s) with a rise time $\tau_r = 0.05\,\text{T}_{\text{dur}}$.

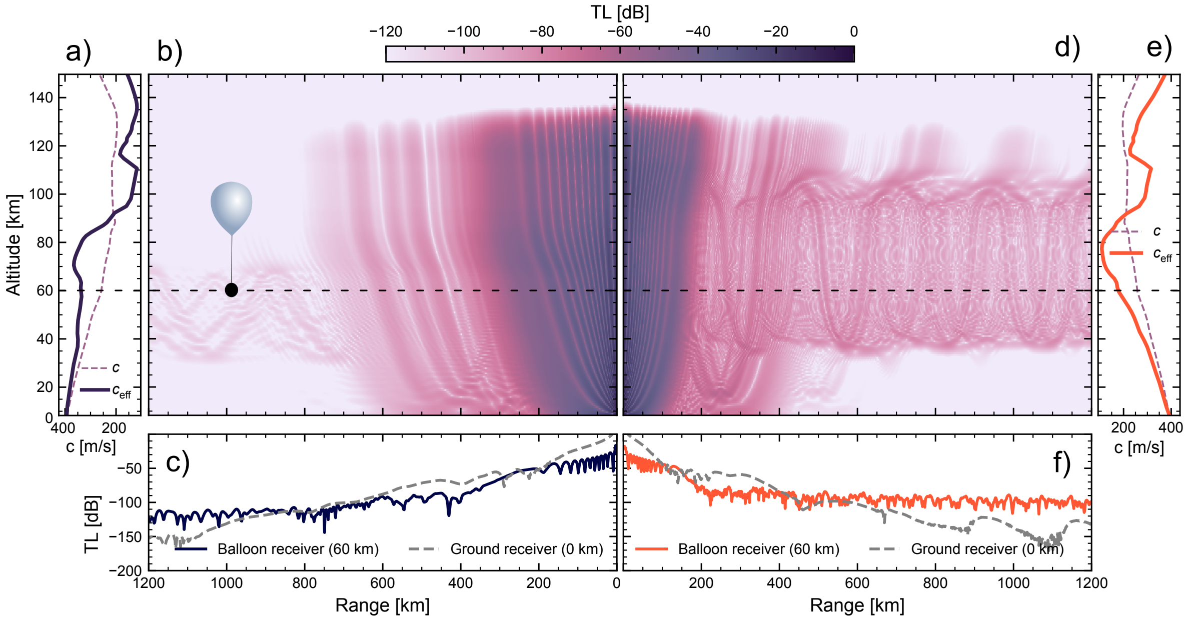

Figure 3. An illustration of the zonal waveguides from the location of Maat Mons during dawn (19:00 UST), towards the west **(a,b,c)** and east **(d,e,f)**. The 0.25 Hz acoustic source is placed at the top of Maat Mons (8.2 km above the mean radius of Venus). The 1D sound speed profiles **(a, e)** are from the first profile along each 2D atmospheric slice. The dashed horizontal black line represent the balloon altitude of 60 km. The bottom panels **(e,f)** shows the corresponding TL for receivers at balloon altitude (solid lines) and the the ground (dashed gray lines). Note that for visualization purposes, the TL in panels **(a,b)** are scaled with the square root of the density which increases the values higher up in the atmosphere.

3 Results

In Figure S2.2, we show the global ducting fractions for rays that hit the ground (Fig. S2.2a) and rays that get trapped around balloon altitude (Fig. S2.2b). The only regions that allow for ground-to-ground propagation within the strict ray-based tau-p framework are found in polar regions around ±60° latitude. This is caused by the SS-AS winds increasing along the solar terminator and towards the poles (see Fig. 1d). In contrast, the trapped ducting fractions show that a large fraction of rays are trapped in elevated waveguides around the balloon, with fractions exceeding 0.2 globally. Keep in mind that the ducting fractions are averaged over all azimuths, meaning that they cannot display directional information.

The trapped tau-p rays indicate strong elevated waveguides that only reach the ground in rare cases. However, as mentioned, frequency-dependent effects such as diffraction might still allow volcanic infrasound to leak into these waveguides, enabling ground-to-ground propagation. For example, wave propagation at 0.25 Hz from Maat Mons, the tallest volcano on Venus, shows a clear coupling with a large waveguide between 30 and 100 km altitude (Fig. 3b). In addition, a weaker coupling is seen towards the west between 30 and 70 km (Fig. 3a). Importantly, the elevated waveguides in both directions encompass the proposed balloon altitude of 60 km. For a similar illustration of the meridional waveguides, see Supplementary Sec. S4.

To explore the global morphology of waveguides on Venus, we ran reciprocal TL computations, i.e., where wind directions are flipped along a given azimuth, from an extensive set of possible balloon locations. Reciprocal simulations enable us to estimate TL from a large number of source-receiver distances from a given balloon location. Figure 4 shows the average TL at the surface for sources between 1500 and 3000 km from the balloon. To retain directional information, the values are grouped into the four cardinal directions. For waves propagating south (Fig. 4(a–c)) and north (Fig. 4(g–i)), we see a symmetric pattern with higher amplitudes towards the poles following the SS-AS circulation. Similarly, infrasound propagating eastward (Fig. 4(j–l)) is also largely driven by the SS-AS circulation, increasing towards the day-night terminator. Lastly, the amplitudes of infrasound propagating west (Fig. 4(d–f)) are driven by the westward global RSR winds in the lower-to-middle atmosphere. The lower altitude of the westward waveguide, means that it experiences less attenuation, although leakage might not be as strong (see Fig. 3). Over a Venus day, each waveguide shifts with the position of the sun in the sky (see Supplementary Sec. S4), due to the stability of the RSR winds and the sun-driven SS-AS circulation. Further, the inclusion of range dependence in the model (see Supplementary Sec. S3) is found to aid the formation of stronger waveguides, while changing balloon altitudes between 50-, 60- and 70 km were not found to have a notable impact on propagation conditions (see Supplementary Sec. S4). Increasing frequency can lead to larger TL peaks, but tend to have lower average TL across balloon locations i.e., attenuation generally suppresses high frequency waves, but local and small-scale wind patterns may create conditions more suitable for shorter wavelengths. Interestingly, the mean TL values follow the same pattern of peaks in trapped ducting fractions (see

Supplementary Sec. S2), which suggests that there is energy leakage between high-altitude waveguides and the surface.

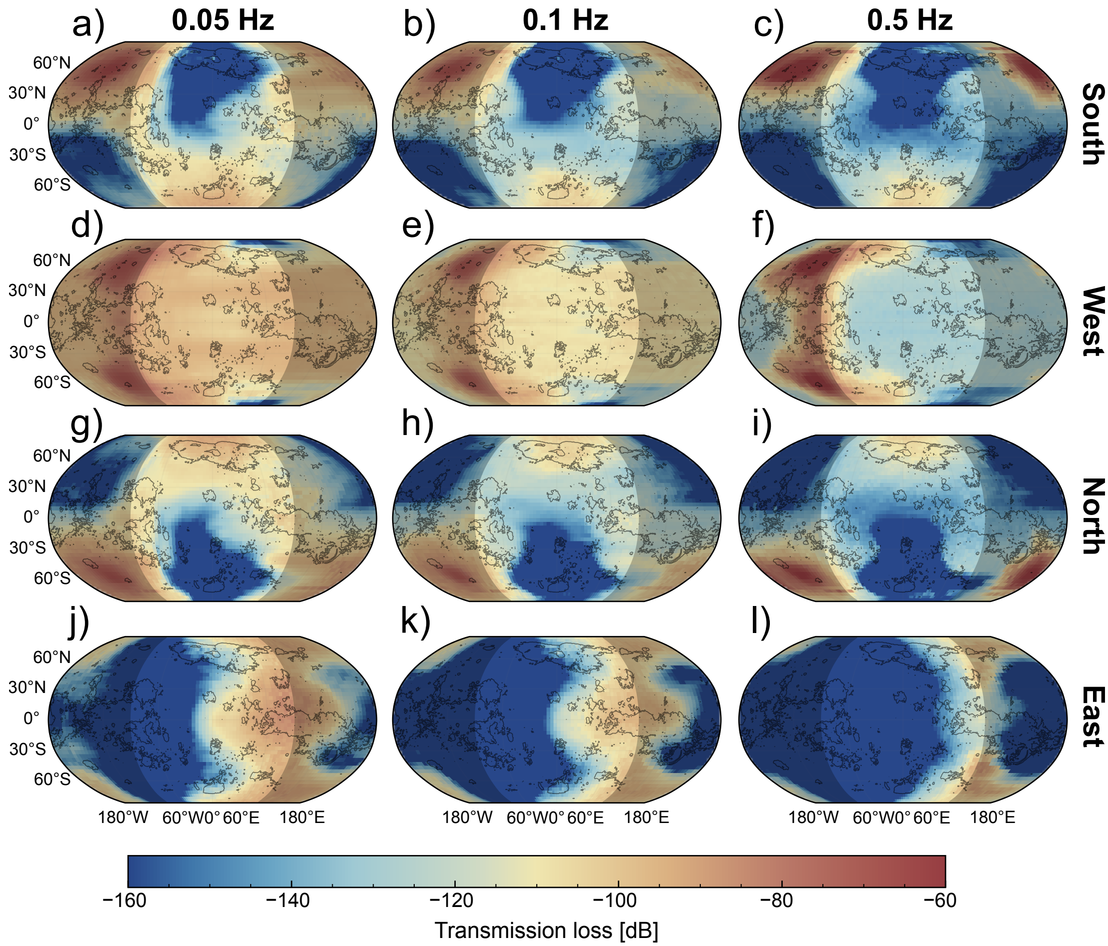

Figure 4. The global morphology of infrasound transmission loss on Venus. The mean Transmission loss between 1500 and 3000 km from ground sources to balloons at 60 km altitude. The panels results are split into different propagation directions: Towards the south (315° to 45°, **(a,b,c)**), the west (45° to 135°, **(d,e,f)**), the north (135° to 225°, **(g,h,i)**) and the east (225° to 315°, **(j,k,l)**). The simulation is done reciprocally i.e., a high value towards the north means that a balloon at that location would be more likely to detect sources located further south. The columns correspond to frequencies 0.05 Hz **(a,d,g,j)**, 0.1 Hz **(b,e,h,k)**and 0.5 Hz **(c,f,i,l)**. All results are calculated at 12:00 UST.

The TL computations (Fig. 4) enable us to determine the main constraints behind the detectability of explosive volcanic eruptions on Venus. Figure 5 shows the minimum detectable peak source pressure (a–c), the number of detectable eruptions (d–f), and the maximum detectable range (g–i) at 12:00 UST. We have assumed a noise level of $\sigma_n = 10^{-2}$ Pa (*Brissaud et al.*, 2026; *Garcia et al.*, 2024) and, for panels (d–i), a peak source pressure of 1000 Pa. Each pixel on the maps represents a possible balloon location. Detecting volcanic signals becomes more challenging (i.e., increase of the minimum detectable source pressure and detectable range from the source, as well as decrease of detectable volcanoes) with increasing frequency when the balloon is located far away from volcanic hotspots (e.g., 0°N 120°E, during dawn). However, the higher TL peaks at 0.5 Hz (Fig. 4(c,f,i,l)) create better conditions where they coincide with volcanic clusters (e.g., 50°N 140°E, during night). In the vicinity of each volcano (within 100 km) and in the western regions with large mean TL (Fig. 4) the detectability tends to be favorable across frequencies. In the western region (60–180°W, during dusk and night), the peak pressure is mostly below $\sim 10^2$ Pa which corresponds to detectable VEI below 3 using our VEI-to-pressure model (assuming an eruption time of 10 seconds, see Sec. 2.4). In this region, smaller detectable source pressures coincide with a considerable number of detectable volcanoes (e.g., above 20 around 120°W 60°N, during night). This is important for the detectability of volcanic eruptions, as active volcano locations remain mostly unknown. At low frequency, almost half the possible balloon locations on Venus show a highly favorable detectable range above 10000 km. To put it into perspective, infrasound from the cataclysmic Hunga-Tonga eruption on 15 January 2022 circumnavigated the Earth five times and was recorded by atmospheric balloons (*Podglajen et al.*, 2022).

We can estimate the detection likelihood of at least one volcanic eruption for a given mission duration by injecting the TL estimates into the probabilistic model. To account for the low likelihood of explosive volcanism on Venus due to the intense surface pressure, we investigated two scenarios, considering that: 1) all large volcanoes are active (Fig. 6a), and 2) only large volcanoes above 4 km elevation are active (Fig. 6b). This second scenario attempts to reflect the more likely magma fragmentation for lower ambient pressure (*Airey et al.*, 2015). The impact of only including high-altitude volcanoes on the main detectability constraints are shown in Supplementary Sec. S5). To calculate detection likelihoods, we considered a balloon at 60 km altitude and the same source model for all eruptions with a duration of 15 s and rise and fall times of 0.75 s. The hourly detection

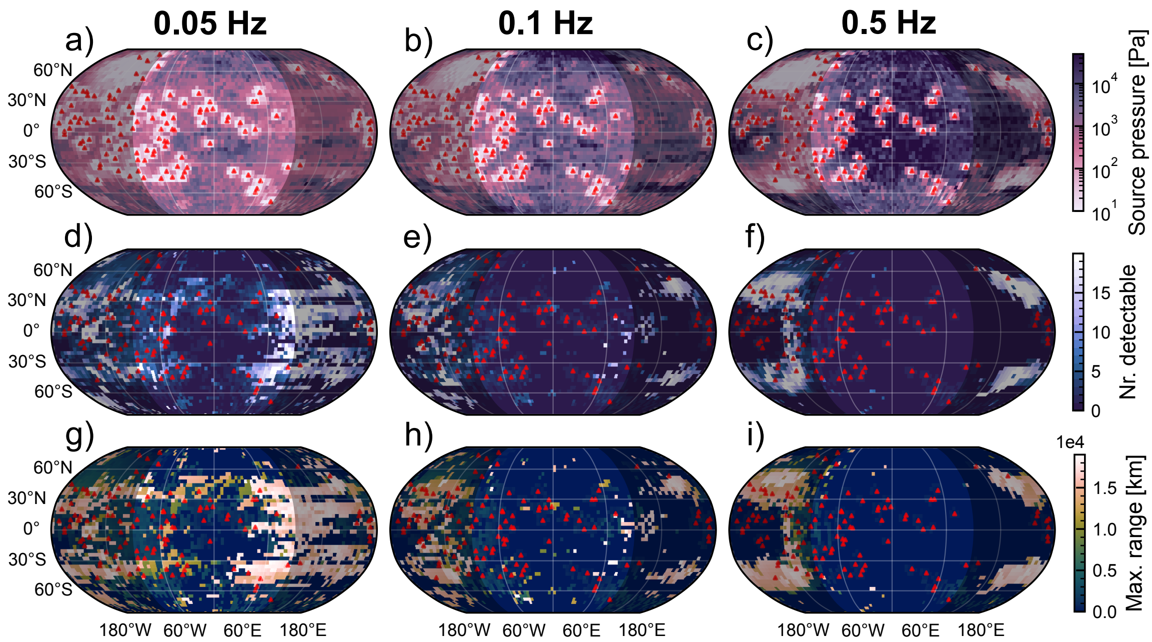

Figure 5. Detectability of explosive volcanic eruptions from a given balloon location at 60 km altitude with a noise level of $\sigma_n = 10^{-2}$ Pa and a SNR threshold of 2. Panels **(a,b,c)** show the minimum detectable peak pressure (Pa) at 1 km from the source, **(d,e,f)** the number of detectable of volcanoes and **(g,h,i)** the maximum detectable range of volcanic eruptions. Both the number of detectable volcanoes and the maximum detectable range is calculated for a peak source pressure of 1000 Pa. Results are shown at 0.05 Hz **(a,d,g)**, 0.1 Hz **(b,e,h)**, and 0.5 Hz **(c,f,i)**. All results are calculated at 12:00 UST. The red triangles indicate the set of large volcanoes from *Hahn and Byrne* (2023).

estimates for each frequency (Fig. 6c-h) peak in the vicinity of volcanoes at night near latitudes 45°N and 45°S and also close to the equator at 0.05 Hz, which were also highlighted by the peaks in maximum detectable range (Fig. 6c,f,i). Interestingly, detection peaks are not always in the vicinity of volcanoes but can also emerge in regions with strong long-range wave ducts that can propagate acoustic energy from distant volcanoes (e.g., around 135°W and 45°S or 135°E and 45°N in Fig. 6h). Outside of these hotspots, and beyond 50 to 100 km from each volcano, hourly detection probabilities drop close to zero, which highlights the importance of long range waveguides to support detectability especially at high frequency. Peaks in hourly detection probability decrease by more than 80 % across all frequencies when considering the smaller number of high altitude volcanoes (Fig. 5f-h).

Integrated over a balloon trajectory (the trajectory is displayed in Fig. 6b), the detection probability reaches values above 99 % at 0.05 Hz and 0.5 Hz after 6 months for SNR = 2 when all the volcanoes are active (Fig. 6i-k). The lowest final probabilities are produced at 0.1 Hz (Fig. 6j) corresponding to an intermediate scenario between well-formed ducts at high frequency (Fig. 6e,h) and low attenuation at low frequency (Fig. 6c,f). The steep increase in detection probabilities at 0.5 Hz (e.g., around UST 21h in Fig. 6k) corresponds to the balloon floating in regions with strong wave ducts which depends both on location and time. The significantly lower number of high altitude volcanoes leads to a 40 % to 75 % drop in final detection probability (Fig. 6i,j,k). Increasing the signal SNR requirement – meaning that only the events producing a higher SNR are included – lowers the final detection probability by about $10-20$ % from SNR 2 to 5. Indeed, strong signals correspond to higher VEI, and are therefore less frequent.

The amplitude model defined in Eq. 9 is dependent on various parameters including eruption time parameters, as well as balloon drop-off latitude, which will impact detection probabilities (see Supplementary Sec. S6). Figure 7 shows the final detection probability for a 6-month mission for a variety of active volcano locations, frequency, total eruption time $\mathrm{T_{dur}}$, and drop-off latitudes. For simplicity, we use a rise time that depends on total duration $\tau_r = 0.05\,\mathrm{T_{dur}}$. Larger detection probabilities occur at higher frequency (Fig. 7ad and Fig. 7c,f) and for a higher density of volcanoes (Fig. 7d-f) as observed for a specific balloon path (Fig. 6i-k). We note a slight asymmetry in detection probability between north and south latitudes, especially at high frequency (Fig. 7c,f), likely due to the time dependence of the trajectories and locations of peaks in hourly detection. After a 6-month mission, the probability is above 90 % for all frequencies and eruption times below 15 s, which suggests a high confidence in the detection of the volcanic-induced infrasound signals when all volcanoes are active. However, we note a strong decay of detection probabilities for longer eruption duration times (or longer rise times, e.g., Fig. 7a,b). Indeed, for a given eruption magnitude, shorter eruption times lead to a larger mass flux rate, and therefore a higher pressure at the source.

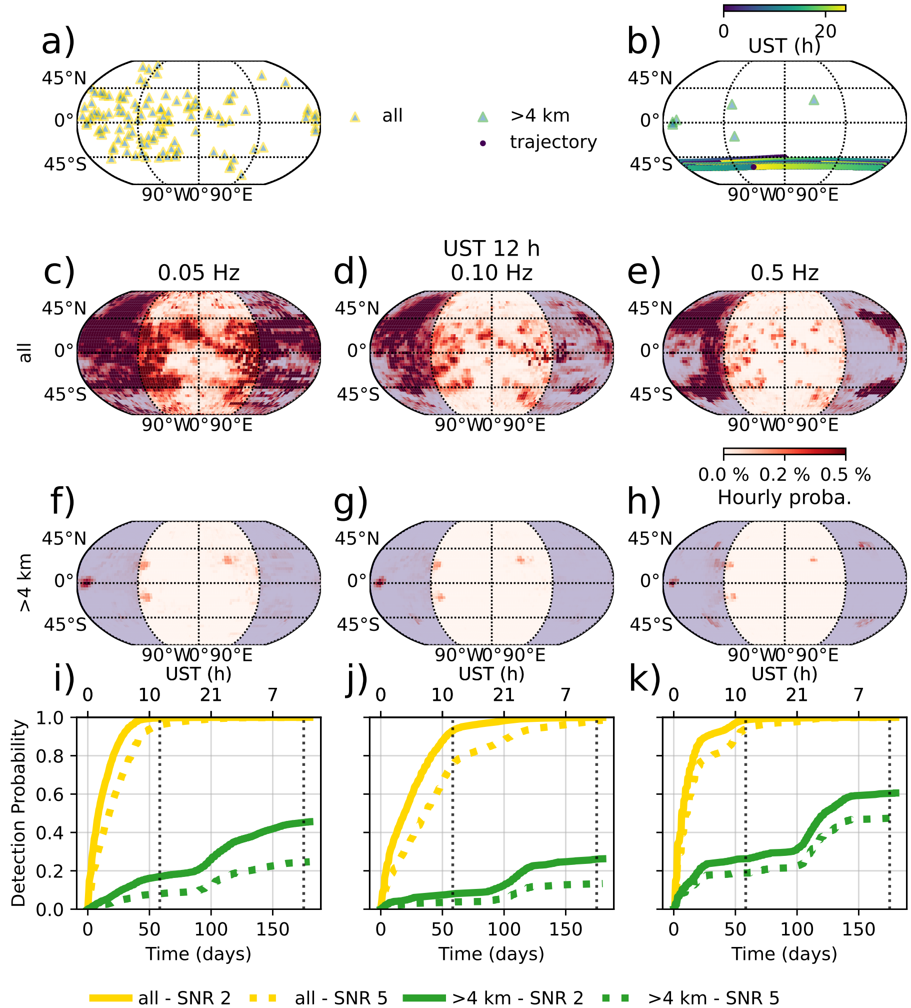

Figure 6. Detection probabilities of volcanic eruptions on Venus. Location of **(a)** all large volcanoes and **(b)** large volcanoes above 4 km elevation along with the balloon trajectory at 60 km altitude from a starting location of (45°S, 0°E). Hourly detection probabilities at UST = 12 h, for a target SNR = 2, for all large volcanoes **(c,d,e)** and large volcanoes above 4 km altitude **(f,g,h)** at frequencies 0.05 Hz **(c,f,i)**, 0.1 Hz **(d,h,j)**, and 0.5 Hz **(e,h,k)**. Nighttime is shown as a dark blue shaded area. Predictions are given for the same source model for all eruptions with a duration of 15 s and rise and fall times of 0.5 s. **(l,m,b)** Detection probabilities integrated along the balloon trajectory, shown in panel **(b)**, for large and intermediate volcanoes (yellow) and large volcanoes only (green) for SNR = 2 (solid line) and SNR = 5 (dotted line). Black dotted vertical lines correspond to UST = 12 h.

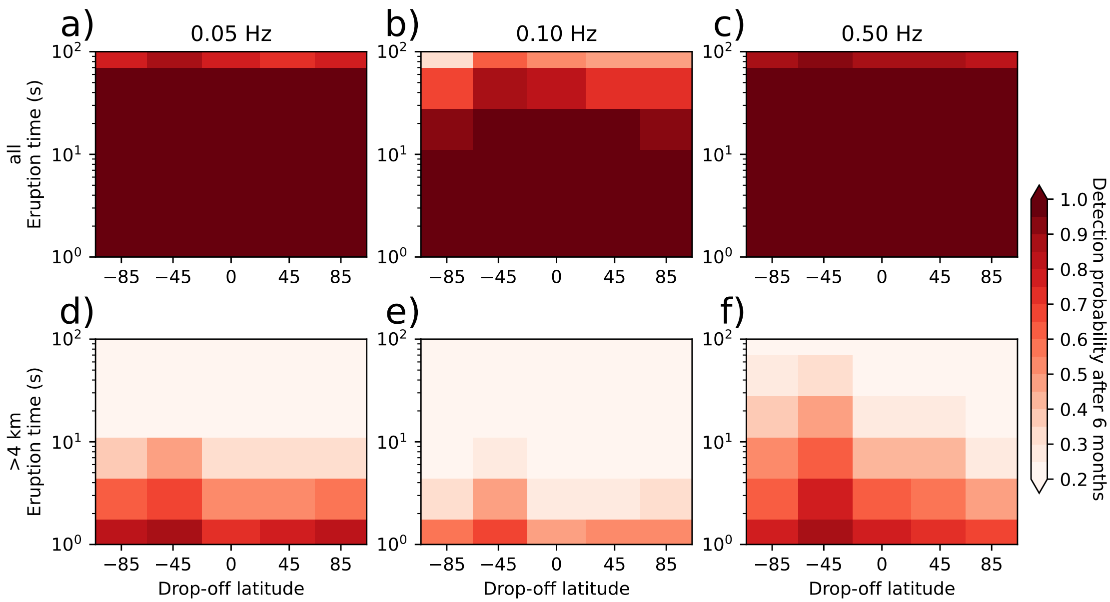

Figure 7. Final detection probability for a target SNR = 5 after a 6-month mission. Detections probabilities are shown vs drop-off latitude and eruption time T_{dur} (s) for all volcanoes **(a,b,c)** and volcanoes above 4 km altitude **(d,e,f)** at 0.05 Hz **(a,d)**, 0.1 Hz **(b,e)**, and 0.5 Hz **(c,f)**.

4 Discussion and limitations

The high final detection probabilities after 6 months when all large volcanoes are active (above 90% for most source and flight parameters), especially at high frequency (Fig. 7c), highlight the potential of balloon missions for volcanic source detections. However, probabilities drop below 80 % for short eruption times (< 5 s) and below 30% for longer eruption times (> 20 s) when only considering active volcanoes above 4 km altitude. Yet, the maximum values of the peak mass rates derived from our source model for eruption magnitudes below 6 (Fig. 2c) are typically lower than those investigated by *Lefèvre et al.* (2025) to trigger explosive volcanism with high-altitude plumes, i.e., plumes reaching above 10 km altitude that can inject acoustic energy efficiently within the atmospheric waveguides (see Supplementary Sec. S4). Similarly, the exit velocities (Fig. 2c,d), for large-vent radius volcanoes, show lower values compared to what was explored in *Lefèvre et al.* (2025). In particular, in our model, events with eruption magnitudes below 3 correspond to peak mass rates below the threshold (about 10^7 kg/s) to obtain high-altitude plumes as identified in *Lefèvre et al.* (2025) for exit velocities below 340 m/s and temperature below 1600 K. Since 97 % of the eruptions considered in our model are below magnitude 3 (Fig. 2a), this suggests that our detectability estimates are likely overly-optimistic since it includes events with low potential for explosive behavior.

The yearly rates used in our probabilistic framework are scaled values from Earth VEI data (*Byrne and Krishnamoorthy*, 2022) which lack calibration from in-situ Venus volcanic event observations. Moreover, VEI are a qualitative measurement of eruption intensity which requires a mapping to physical units such as eruption magnitude (Sec. 2.4). An alternative to VEI would be to scale eruption magnitudes directly from Earth to Venus using the approach of *Byrne and Krishnamoorthy* (2022). Together with yearly rate estimates, we assumed that all or a subset of large volcanic edifices identified from Magellan data (*Hahn and Byrne*, 2023) are equally active. This is a strong and likely unrealistic assumption that would lead to smaller detection probabilities if there are less active volcanoes and/or less activity per active volcano. Finally, we made a critical assumption that our source can be approximated by an isotropic mass-driven model. This neglects highly-directional volcanic jets and acoustic waves produced by plume convection. Some of the acoustic-gravity wave patterns recorded during the 15 January 2022 Hunga Tonga Hunga Ha'Apai eruption have been proposed to originate from its plume and umbrella cloud (*Zhang et al.*, 2025b; *Gullbekk*, 2025). Although this source mechanism is not well understood, it could play an important role in the infrasound-based detection of active eruptions on Venus. TL estimates using elevated sources above the surface highlight that large plumes above 20 km altitude would show higher detection probabilities, compared to lower altitude sources, as they would deposit energy directly within the Venus atmospheric waveguides (SI S5).

Beyond the source model, the path effects included here rely on parabolic equation simulations which ignore important aspects, namely: 1) nonlinear wave breaking near the vent and at high altitudes, 2) cross winds, i.e, winds orthogonal to the direction of propagation, 3) vertical winds, 4) the effective sound speed and shallow angle approximation, 5) wave propagation in near-critical fluids, and 6) Venus sphericity and global-scale propagation. Nonlinear wave breaking leads to large high-frequency amplitudes followed by a significant attenuation as the wave travels through the atmosphere, resulting in lower wave amplitudes than when modeled in the linear regime at large distances from the source. Although crosswinds can slightly alter wave paths over large distances, they typically do not significantly alter amplitudes at low frequencies. Similarly, the influence of vertical winds is typically assumed to be minimal on wave characteristics (*Drob et al.*, 2003) but they could impact both balloon trajectories and noise levels (*Krishnamoorthy et al.*, 2020). We assumed the atmosphere to be an ideal fluid, which is unrealistic in the deep atmosphere of Venus, where thermal and convective instabilities could influence the sound propagation (*Averbuch et al.*, 2023). Finally, we only simulated acoustic propagation in a Cartesian domain up to 3000 km distance from the source to reduce the computational cost. For larger distances, we performed a linear extrapolation of TL data, in db, fitted from a 1000 to 3000 km. However, the linear fits assumes the impact of atmospheric parameter variations is not significant on TL amplitudes at a global scale. Numerical methods accounting accounting for a planet's curvature would be preferred in future studies (e.g., *Zhang et al.*, 2025a).

Noise levels on Venus, primarily driven by atmospheric convection, balloon-induced vortex shedding, tether resonance, wave-induced balloon oscillations, and wave scattering on the balloon envelope, remain largely unconstrained. The real noise amplitudes might differ by an order of magnitude from the estimate we used, which is 10^{-2} Pa. Higher noise levels would naturally yield lower detection probabilities. This can be explored within our framework by looking at higher target SNR, where, for example, doubling the noise level would be equivalent to doubling the target SNR. In this example, following Fig. 6i,j, final detection probabilities would be 20 % lower below 0.1 Hz.

Due to the sparse observations of the Venusian atmosphere, particularly below the clouds, the profiles from the VCD will contain significant biases. Further, atmospheric variables in the VCD are available only hourly. In addition, its wind and temperature fields do not contain small-scale perturbations that exist on Earth due to gravity-wave effects and which have been shown to greatly enhance long-range infrasound propagation (e.g., *Norris and Gibson*, 2002; *Vorobeva et al.*, 2023; *Listowski et al.*, 2024; *Cameijo et al.*, 2025). Similar gravity-waves have been observed in the cloud layer by the Venus Express and Akatsuki missions (*Sugimoto et al.*, 2021). One scenario is that a prospective presence of smaller-scale wind and temperature variations, currently not resolved in the VCD, enhances the actual infrasound ducting on Venus. Further, effects caused by the different EUV and cloud albedo scenarios in the VCD are not considered but known to affect both the RSR and SS-AS winds.

5 Conclusions

We apply a novel framework to investigate global infrasound wave propagation morphology and volcanic event detectability on a balloon platform on Venus. This framework is based on numerical propagation simulations and the VCD representation of Venus's atmosphere. We addressed two key research questions related to the feasibility of balloon-borne acoustic monitoring of explosive volcanism on Venus: 1) Does Venus's atmospheric structure support the formation of long-range infrasonic waveguides from volcanoes to upper-atmospheric balloons? 2) Given an assumed set of active volcanoes, how likely are explosive eruptions to be detected over a long-duration balloon mission?

We have identified strong and previously unknown high-altitude waveguides on Venus. These wind-driven waveguides allow for long-range ducting and volcanism-generated infrasound detection at balloon-borne acoustic sensors. For example, at Maat Mons, the highest volcano edifice on Venus, acoustic waves can be trapped in a waveguide between 40 and 100 km altitudes towards the East and 40 and 70 km altitudes towards the west (Fig. 3) similar to the AtmoSOFAR channel on Earth (*Albert et al.*, 2023). We quantified the strength of such waveguides by computing average TL towards balloon locations in different back-azimuth and distance bins (Fig. 4). The TL peaks are distributed along the day-night terminators and at high latitudes with high TL at high frequency, but with larger average values across the whole planet at low frequency. At 0.5 Hz, volcanic eruptions with a peak source pressure of 1000 Pa can be detected more than 15000 km away for a target $\mathrm{SNR} = 2$, allowing for near-global detectability of volcanic events (Fig. 5).

In order to statistically assess the detectability of Venus explosive volcanism, we modeled these sources under the assumption of an isotropic source, driven by mass-injection into the atmosphere (eq. 9). These assumptions produce a set of realistic values for peak mass rates and exit velocities (Fig. 2). We obtained very high detection probabilities after a 6-month balloon mission (above 90%) when all large volcanoes on Venus are active and producing explosive volcanism (Fig. 7a-c). However, the final detection probabilities drop significantly when only considering high-altitude volcanoes where the ambient pressure is low and which are more likely to enable explosive volcanism (Fig. 7d-f). In particular, our volcano amplitude model suggests that only small eruption times (below 5 s), i.e., releasing energy quickly, lead to acceptable detectability values for a planetary mission above 60% after 6 months.

Our probabilistic framework confirms that balloon missions are likely to detect volcanic events for several combinations of source and propagation parameters. High detection probabilities are due to the presence of high-altitude acoustic waveguides. However, such detections would be highly dependent on the temporal and spatial distribution of explosive eruptions on Venus and their characteristics, especially their magnitude. Future studies could attempt to refine the set of atmospheric and geological parameters that enable explosive volcanism on Venus through volcanic dynamics conduit modeling, as initiated by *Lefèvre et al.* (2025). Fluid simulations would enable extraction of the emitted acoustic energy at the source, including explosion, jet, and plume acoustic generation processes. Importantly, data from the synthetic aperture radar instruments part of the already funded space missions VERITAS and EnVision will provide surface data with unprecedented resolution, enabling the identification of eruption-related changes (*Smrekar et al.*, 2022; *Widemann et al.*, 2022) and help further constraining the source model parameters. Detection is an important milestone, but localization and inversion of source parameters, such as erupted mass or plume geometry, from balloon-borne infrasound signals should be the next step. In particular, constraining uncertainties in the inversion of source parameters from volcano-induced infrasound will be key to ensuring the success of future missions, as explored for earthquake-induced acoustic waves (*Froment et al.*, 2025). Beyond volcanic sources, our framework would also enable the investigation of fireball fragmentation and lightning detection that could both emit acoustic waves in Venus' cloud layer (*Blaske et al.*, 2023; *Christou and Gritsevich*, 2024).

Acknowledgements

The authors would like to thank Tyler Paladino and Alexa Van Eaton from the USGS Cascades Volcano Observatory for fruitful discussions on the development of our volcano source model. We are also grateful for the helpful feedback received from Tyler Paladino and another USGS internal reviewer on a previous version of the manuscript. This work received support from the *Airborne Inversion of Rayleigh waves* (AIR) project, funded by the Research Council of Norway basic research program FRIPRO, Contract 335903. We thank the Norwegian national e-infrastructure for computational science, Sigma2, for providing high-performance computational resources through the University of Oslo Project number NN8104K. Several results in the current paper were first presented in the MSc thesis *The Global Morphology of Infrasound on Venus: Propagation from Volcanic Sources to Balloon-borne Sensors* (*Gullbekk*, 2025). Any use of trade, firm, or product names is for descriptive purposes only and does not imply endorsement by the U.S. Government

Author contributions

Conceptualization: Q.B., S.P.N., M.F., S.B.G.
Supervision: S.P.N., M.F., Q.B.
Methodology and Formal analysis: S.B.G., Q.B., M.F., S.P.N.
Investigation: S.B.G., Q.B., M.F., S.P.N., M.L., A.M.I.
Validation: S.B.G., Q.B.
Visualization: S.B.G., Q.B.
Writing – original draft: S.B.G., Q.B., M.F., S.P.N.
Writing – review and editing: S.B.G., Q.B., M.F., S.P.N., M.L., A.M.I.

Competing interests

The authors declare that they have no competing interests.

Open Research

The code to generate probabilistic estimates can be found at https://github.com/QuentinBrissaud/Venus_Detectability_Volcanoes. The TL data will be made available upon paper acceptance. The Venus Climate Database (VCD) is available at http://www-venus.lmd.jussieu.fr/info_web/index.html (*Lebonnois et al.*, 2010, 2016; *Martinez et al.*, 2023). The spatial distribution of volcanoes on Venus is extracted from the *Global Catalog of Volcanoes and Volcanic Fields on Venus* (*Hahn and Byrne*, 2023). These data are openly available at https://data.library.wustl.edu/record/102?v=zip. The finite-frequency simulations use the parabolic equation solver ePape, which is part of the NCPAprop software package (*Waxler et al.*, 2021; *Waxler and Assink*, 2018). This code is available at https://github.com/chetzer-ncpa/ncpaprop-release?tab=readme-ov-file. The ray tracing simulations, only used in the ray-path visualization of Fig. S2.1in Supplementary Sec. S2, are performed using the infraGA code (*Blom*, 2025; *Blom and Waxler*, 2021), available at https://github.com/LANL-Seismoacoustics/infraGA. Figures in this article were produced with the Matplotlib and Cartopy Python modules, using colormaps made available to the community by Fabio Crameri (*Crameri et al.*, 2020), provided at https://www.fabiocrameri.ch/colourmaps/.

References

Airey, M. W., T. A. Mather, D. M. Pyle, L. S. Glaze, R. C. Ghail, and C. F. Wilson (2015), Explosive volcanic activity on Venus: The roles of volatile contribution, degassing, and external environment, *Planetary and Space Science*, *113–114*, 33–48, https://doi.org/10.1016/j.pss.2015.01.009.

Albert, S., D. Bowman, E. Silber, and F. Dannemann Dugick (2023), The atmosofar channel: First direct observations of an elevated acoustic duct, *Earth and Space Science*, *10*(10), e2023EA003,149, https://doi.org/10.1029/2023EA003149.

Assink, J., R. Waxler, and D. Velea (2017), A wide-angle high mach number modal expansion for infrasound propagation, *The Journal of the Acoustical Society of America*, *141*(3), 1781–1792, https://doi.org/doi.org/10.1121/1.4977578.

Averbuch, G., R. Houston, and A. Petculescu (2023), Seismo-acoustic coupling in the deep atmosphere of Venus, *The Journal of the Acoustical Society of America*, *153*(3), 1802–1810, https://doi.org/10.1121/10.0017428.

Blaske, C. H., J. G. O'Rourke, S. Desch, and M. E. Borrelli (2023), Meteors may masquerade as lightning in the atmosphere of Venus, *Journal of Geophysical Research: Planets*, *128*(9), e2023JE007,914, https://doi.org/10.1029/2023JE007914.

Blom, P. (2025), InfraGA: Modeling propagation of infrasound in the limit of geometric acoustics, https://github.com/LANL-Seismoacoustics/infraGA, accessed: 2026-04-06.

Blom, P., and R. Waxler (2021), Characteristics of thermospheric infrasound predicted using ray tracing and weakly non-linear waveform analyses, *The Journal of the Acoustical Society of America*, *149*(5), 3174–3188, https://doi.org/10.1121/10.0004949.

Brissaud, Q., S. P. Näsholm, A. Turquet, and A. Le Pichon (2023), Predicting infrasound transmission loss using deep learning, *Geophysical Journal International*, *232*(1), 274–286, https://doi.org/10.1093/gji/ggac307.

Brissaud, Q., C. Kong, M. Froment, J. Wilding, A. J. Gülcher, J. M. Jackson, I. van Zelst, R. F. Garci, C. M. Solberg, and S. P. Näsholm (2026), Aerial and space-borne seismology on venus: Viability and design implications for future missions, *Earth and Space Science*, *13*(6), e2025EA004,541, https://doi.org/10.1029/2025EA004541.

Byrne, P. K., and S. Krishnamoorthy (2022), Estimates on the frequency of volcanic eruptions on Venus, *Journal of Geophysical Research: Planets*, *127*(1), e2021JE007,040, https://doi.org/10.1029/2021JE007040.

Cameijo, A. J., A. Le Pichon, Y. Sklab, S. Arib, Q. Brissaud, S. Näsholm, C. Listowski, and S. Aknine (2025), Toward real-time assessment of infrasound event detection capability using deep learning-based transmission loss estimation, *Journal of Geophysical Research: Atmospheres*, *130*(19), e2025JD043,577, https://doi.org/10.1029/2025JD043577.

Campbell, B. A., G. A. Morgan, J. L. Whitten, L. M. Carter, L. S. Glaze, and D. B. Campbell (2017), Pyroclastic flow deposits on Venus as indicators of renewed magmatic activity, *Journal of Geophysical Research: Planets*, *122*(7), 1580–1596, https://doi.org/10.1002/2017JE005299.

Carcione, J. M. (2007), *Wave fields in real media: Wave propagation in anisotropic, anelastic, porous and electromagnetic media*, vol. 38, Elsevier, https://doi.org/10.1016/C2013-0-18893-9.

Christou, A. A., and M. Gritsevich (2024), Feasibility of meteor surveying from a Venus orbiter, *Icarus*, *417*, 116,116, https://doi.org/10.1016/j.icarus.2024.116116.

Clague, D. A., J. B. Paduan, and A. S. Davis (2009), Widespread strombolian eruptions of mid-ocean ridge basalt, *Journal of Volcanology and Geothermal Research*, *180*(2), 171–188, https://doi.org/10.1016/j.jvolgeores.2008.08.007.

Crameri, F., G. E. Shephard, and P. J. Heron (2020), The misuse of colour in science communication, *Nature communications*, *11*(1), 5444, https://doi.org/10.1038/s41467-020-19160-7.

Crone, T. J., and D. R. Bohnenstiehl (2019), Acoustic evidence of a long-lived gas-driven submarine volcanic eruption in the Bismarck Sea, *Geophysical Journal International*, *217*(1), 169–178, https://doi.org/10.1093/gji/ggy542.

Cutts, J. A., M. H. Hecht, K. J. Horn, J. S. Izraelevitz, and S. Krishnamoorthy (2025), Extending the lifetime of Venus aerobots with CO2 electrolysis: Implications for seismic exploration, in *56th Lunar and Planetary Science Conference*, vol. 3090, p. 2751.

Dabrowa, A., D. Green, A. Rust, and J. Phillips (2011), A global study of volcanic infrasound characteristics and the potential for long-range monitoring, *Earth and Planetary Science Letters*, *310*(3), 369–379, https://doi.org/10.1016/j.epsl.2011.08.027.

Drob, D. P., J. M. Picone, and M. Garcés (2003), Global morphology of infrasound propagation, *Journal of Geophysical Research: Atmospheres*, *108*(D21), https://doi.org/10.1029/2002JD003307.

Drob, D. P., M. Garcés, M. Hedlin, and N. Brachet (2010), The Temporal Morphology of Infrasound Propagation, *Pure and Applied Geophysics*, *167*(4), 437–453, https://doi.org/10.1007/s00024-010-0080-6.

Fagents, S. A., and L. Wilson (1995), Explosive volcanism on Venus: Transient volcanic explosions as a mechanism for localized pyroclast dispersal, *Journal of Geophysical Research: Planets*, *100*(E12), 26,327–26,338, https://doi.org/10.1029/95JE03202.

Fee, D., and R. S. Matoza (2013), An overview of volcano infrasound: From hawaiian to plinian, local to global, *Journal of Volcanology and Geothermal Research*, *249*, 123–139, https://doi.org/10.1016/j.jvolgeores.2012.09.002.

Filiberto, J., M. Y. Zolotov, E. Kohler, P. D'Incecco, D. A. Gorinov, S. S. Bhiravarasu, M. B. Weller, J. F. Brossier, I. López, P. J. Mason, J. A. Edmond, N. Mari, G. Komatsu, G. Di Achille, and J. B. Garvin

(2025), Assessing the evidence for active volcanism on Venus: Current limitations and prospects for future investigations, *Geochemistry*, *85*(4), 126,316, https://doi.org/10.1016/j.chemer.2025.126316.

Froment, M., Q. Brissaud, S. P. Näsholm, and J. Schweitzer (2025), Balloon seismology enables subsurface inversion without ground stations, *Communications Earth & Environment*, *6*(1), 949, https://doi.org/10.1038/s43247-025-02917-7.

Galetto, F., M. E. Pritchard, A. J. Hornby, E. Gazel, and N. M. Mahowald (2023), Spatial and Temporal Quantification of Subaerial Volcanism From 1980 to 2019: Solid Products, Masses, and Average Eruptive Rates, *Reviews of Geophysics*, *61*(1), e2022RG000,783, https://doi.org/10.1029/2022RG000783.

Ganesh, I., L. M. Carter, and T. N. Henz (2022), Radar Backscatter and Emissivity Models of Proposed Pyroclastic Density Current Deposits on Venus, *Journal of Geophysical Research: Planets*, *127*(10), e2022JE007,318, https://doi.org/10.1029/2022JE007318.

Garcés, M. A., R. A. Hansen, and K. G. Lindquist (1998), Traveltimes for infrasonic waves propagating in a stratified atmosphere, *Geophysical Journal International*, *135*(1), 255–263, https://doi.org/10.1046/j.1365-246X.1998.00618.x.

Garcia, R. F., Q. Brissaud, L. Rolland, R. Martin, D. Komatitsch, A. Spiga, P. Lognonné, and B. Banerdt (2017), Finite-difference modeling of acoustic and gravity wave propagation in Mars atmosphere: application to infrasounds emitted by meteor impacts, *Space Science Reviews*, *211*, 547–570, https://doi.org/10.1007/s11214-016-0324-6.

Garcia, R. F., I. van Zelst, T. Kawamura, S. P. Näsholm, A. Horleston, S. Klaasen, M. Lefevre, C. M. Solberg, K. T. Smolinski, A.-C. Plesa, et al. (2024), Seismic wave detectability on Venus using ground deformation sensors, infrasound sensors on balloons and airglow imagers, *Earth and Space Science*, *11*(11), e2024EA003,670, https://doi.org/10.1029/2024EA003670.

Garvin, J. B., J. W. Head, and L. Wilson (1982), Magma vesiculation and pyroclastic volcanism on Venus, *Icarus*, *52*(2), 365–372, https://doi.org/10.1016/0019-1035(82)90119-1.

Ghail, R. C., S. E. Smrekar, T. Widemann, P. K. Byrne, A. J. Gülcher, J. G. O'Rourke, M. E. Borrelli, M. S. Gilmore, R. R. Herrick, M. A. Ivanov, et al. (2024), Volcanic and tectonic constraints on the evolution of Venus, *Space Science Reviews*, *220*(4), 36, https://doi.org/10.1007/s11214-024-01065-2.

Gheri, D., E. Marchetti, R. De Negri, P. Hupe, G. Belli, A. Le Pichon, S. P. Näsholm, and P. Mialle (2025), Detecting explosive volcanism using global long-range infrasound data, *Journal of Volcanology and Geothermal Research*, *462*, 108,320, https://doi.org/10.1016/j.jvolgeores.2025.108320.

Godin, O. A. (1997), Reciprocity and energy theorems for waves in a compressible inhomogeneous moving fluid, *Wave motion*, *25*(2), 143–167, https://doi.org/10.1016/S0165-2125(96)00037-6.

Godin, O. A. (2002), An effective quiescent medium for sound propagating through an inhomogeneous, moving fluid, *The Journal of the Acoustical Society of America*, *112*(4), 1269–1275, https://doi.org/10.1121/1.1504853.

Gullbekk, S. B. (2025), The global morphology of infrasound on Venus: Propagation from volcanic sources to balloon-borne sensors, Master's thesis, University of Oslo, Faculty of Mathematics and Natural Sciences, Department of Informatics, Oslo, Norway, https://hdl.handle.net/11250/5365171.

Hahn, R. M., and P. K. Byrne (2023), A morphological and spatial analysis of volcanoes on Venus, *Journal of Geophysical Research: Planets*, *128*(4), e2023JE007,753, https://doi.org/10.1029/2023JE007753.

Hamilton, M., and D. Blackstock (1998), *Nonlinear Acoustics*, Academic Press.

Head, J. W., D. B. Campbell, C. Elachi, J. E. Guest, D. P. McKenzie, R. S. Saunders, G. G. Schaber, and G. Schubert (1991), Venus volcanism: Initial Analysis from Magellan data, *Science*, *252*(5003), 276–288, https://doi.org/10.1126/science.252.5003.276.

Head, J. W. I., and L. Wilson (1986), Volcanic processes and landforms on Venus: Theory, predictions, and observations, *Journal of Geophysical Research: Solid Earth*, *91*(B9), 9407–9446, https://doi.org/10.1029/JB091iB09p09407.

Helo, C., M.-A. Longpré, N. Shimizu, D. A. Clague, and J. Stix (2011), Explosive eruptions at mid-ocean ridges driven by CO2-rich magmas, *Nature Geoscience*, *4*(4), 260–263, https://doi.org/10.1038/ngeo1104.

Herrick, R. R., and S. Hensley (2023), Surface changes observed on a Venusian volcano during the Magellan mission, *Science*, *379*(6638), 1205–1208, https://doi.org/10.1126/science.abm7735.

Horinouchi, T., T. Kouyama, M. Imai, S.-y. Murakami, Y. J. Lee, A. Yamazaki, M. Yamada, S. Watanabe, T. Imamura, J. Peralta, and T. Satoh (2024), Long-term variability of mean winds and planetary-scale waves around venusian cloud top observed with akatsuki/uvi, *Journal of Geophysical Research: Planets*, *129*(3), https://doi.org/doi.org/10.1029/2023JE008221.

Keddie, S. T., and J. W. Head (1995), Formation and evolution of volcanic edifices on the Dione Regio rise, Venus, *Journal of Geophysical Research: Planets*, *100*(E6), 11,729–11,754, https://doi.org/10.1029/95JE00822.

Krishnamoorthy, S., D. C. Bowman, A. Komjathy, M. T. Pauken, and J. A. Cutts (2020), Origin and mitigation of wind noise on balloon-borne infrasound microbarometers, *The Journal of the Acoustical Society of America*, *148*(4), 2361–2370, https://doi.org/10.1121/10.0002356.

Lalande, J.-M., O. Sèbe, M. Landès, P. Blanc-Benon, R. S. Matoza, A. Le Pichon, and E. Blanc (2012), Infrasound data inversion for atmospheric sounding, *Geophysical Journal International*, *190*(1), 687–701, https://doi.org/10.1111/j.1365-246X.2012.05518.x.

Lebonnois, S., F. Hourdin, V. Eymet, A. Crespin, R. Fournier, and F. Forget (2010), Superrotation of Venus' atmosphere analyzed with a full general circulation model, *Journal of Geophysical Research: Planets*, *115*(E6), https://doi.org/10.1029/2009JE003458.

Lebonnois, S., N. Sugimoto, and G. Gilli (2016), Wave analysis in the atmosphere of Venus below 100-km altitude, simulated by the LMD Venus GCM, *Icarus*, *278*, 38–51, https://doi.org/10.1016/j.icarus.2016.06.004.

Lefèvre, M., M. Cerminara, and A. Costa (2025), Eruption Column Modeling of Explosive Volcanism on Venus, *Journal of Geophysical Research: Planets*, *130*(10), e2025JE009,320, https://doi.org/10.1029/2025JE009320.

Listowski, C., C. C. Stephan, A. Le Pichon, A. Hauchecorne, Y.-H. Kim, U. Achatz, and G. Bölöni (2024), Stratospheric gravity waves impact on infrasound transmission losses across the international monitoring system, *Pure and Applied Geophysics*, https://doi.org/10.1007/s00024-024-03467-3.

Martinez, A., S. Lebonnois, E. Millour, T. Pierron, E. Moisan, G. Gilli, and F. Lefèvre (2023), Exploring the variability of the Venusian thermosphere with the IPSL Venus GCM, *Icarus*, *389*, 115,272, https://doi.org/10.1016/j.icarus.2022.115272.

Moresi, L., and B. Mather (2019), Stripy: A Python module for (constrained) triangulation in Cartesian coordinates and on a sphere., *Journal of Open Source Software*, *4*(38), 1410, https://doi.org/10.21105/joss.01410.

Navarro, T., G. Gilli, G. Schubert, S. Lebonnois, F. Lefèvre, and D. Quirino (2021), Venus' upper atmosphere revealed by a gcm: I. structure and variability of the circulation, *Icarus*, *366*, https://doi.org/doi.org/10.1016/j.icarus.2021.114400.

Newhall, C. G., and S. Self (1982), The volcanic explosivity index (VEI) an estimate of explosive magnitude for historical volcanism, *Journal of Geophysical Research: Oceans*, *87*(C2), 1231–1238, https://doi.org/10.1029/JC087iC02p01231.

Norris, D., and R. Gibson (2002), InfraMAP enhancements: environmental/propagation variability and localization accuracy of infrasonic networks, in *Proceedings of the 24th Seismic Research Review—Nuclear Explosion Monitoring: Innovation and Integration*, pp. 809–813.

Perttu, A., C. Caudron, J. Assink, D. Metz, D. Tailpied, B. Perttu, C. Hibert, D. Nurfiani, C. Pilger, M. Muzli, et al. (2020), Reconstruction of the 2018 tsunamigenic flank collapse and eruptive activity at Anak Krakatau based on eyewitness reports, seismo-acoustic and satellite observations, *Earth and Planetary Science Letters*, *541*, 116,268, https://doi.org/10.1016/j.epsl.2020.116268.

Petculescu, A. (2016), Acoustic properties in the low and middle atmospheres of Mars and Venus, *The Journal of the Acoustical Society of America*, *140*(2), 1439–1446, https://doi.org/10.1121/1.4960784.

Piñeyro, B., R. Sabatini, and J. B. Snively (2026), Impact of species diffusion on the attenuation of acoustic waves in multi-component planetary atmospheres, *The Journal of the Acoustical Society of America*, *159*(2), 1721–1748, https://doi.org/10.1121/10.0042249.

Podglajen, A., A. Le Pichon, R. F. Garcia, S. Gérier, C. Millet, K. Bedka, K. Khlopenkov, S. Khaykin, and A. Hertzog (2022), Stratospheric balloon observations of infrasound waves from the 15 January 2022 Hunga eruption, Tonga, *Geophysical Research Letters*, *49*(19), e2022GL100,833, https://doi.org/10.1029/2022GL100833.

Resing, J. A., K. H. Rubin, R. W. Embley, J. E. Lupton, E. T. Baker, R. P. Dziak, T. Baumberger, M. D. Lilley, J. A. Huber, T. M. Shank, D. A. Butterfield, D. A. Clague, N. S. Keller, S. G. Merle, N. J. Buck, P. J. Michael, A. Soule, D. W. Caress, S. L. Walker, R. Davis, J. P. Cowen, A.-L. Reysenbach, and H. Thomas (2011), Active submarine eruption of boninite in the northeastern Lau Basin, *Nature Geoscience*, *4*(11), 799–806, https://doi.org/10.1038/ngeo1275.

Sánchez-Lavega, A., S. Lebonnois, T. Imamura, P. Read, and D. Luz (2017), The atmospheric dynamics of venus, *Space Science Reviews*, *212*, 1541–1616, https://doi.org/doi.org/10.1007/s11214-017-0389-x.

Schubert, G., S. W. Bougher, C. C. Covey, A. D. Del Genio, A. S. Grossman, J. L. Hollingsworth, S. S. Limaye, and R. E. Young (2007), Venus atmosphere dynamics: A continuing enigma, in *Exploring Venus as a Terrestrial Planet*, *Geophysical Monograph Series*, vol. 176, pp. 101–120, American Geophysical Union, https://doi.org/doi.org/10.1029/176GM07.

Smrekar, S., S. Hensley, R. Nybakken, M. S. Wallace, D. Perkovic-Martin, T.-H. You, D. Nunes, J. Brophy, T. Ely, E. Burt, et al. (2022), VERITAS (Venus emissivity, radio science, InSAR, topography, and spectroscopy): A discovery mission, in *2022 IEEE Aerospace Conference (AERO)*, pp. 1–20, IEEE, https://doi.org/10.1109/AERO53065.2022.9843269.

Sugimoto, N., Y. Fujisawa, H. Kashimura, K. Noguchi, T. Kuroda, M. Takagi, and Y.-Y. Hayashi (2021), Generation of gravity waves from thermal tides in the venus atmosphere, *Nature communications*, *12*(3682), https://doi.org/10.1038/s41467-021-24002-1.

Sulcanese, D., G. Mitri, and M. Mastrogiuseppe (2024), Evidence of ongoing volcanic activity on Venus revealed by Magellan radar, *Nature Astronomy*, pp. 1–10, https://doi.org/10.1038/s41550-024-02272-1.

Sutherland, L. C., and H. E. Bass (2004), Atmospheric absorption in the atmosphere up to 160 km, *The Journal of the Acoustical Society of America*, *115*(3), 1012–1032, https://doi.org/10.1121/1.1631937.

Trahan, A. J., and A. Petculescu (2020), Absorption of infrasound in the lower and middle clouds of Venus, *The Journal of the Acoustical Society of America*, *148*(1), 141–152, https://doi.org/10.1121/10.0001520.

van Zelst, I. (2022), Comment on "Estimates on the frequency of volcanic eruptions on Venus" by Byrne and Krishnamoorthy (2022), *Journal of Geophysical Research: Planets*, *127*(12), e2022JE007,448, https://doi.org/10.1029/2022JE007448.

Vergniolle, S., G. Brandeis, and J.-C. Mareschal (1996), Strombolian explosions: 2. Eruption dynamics determined from acoustic measurements, *Journal of Geophysical Research: Solid Earth*, *101*(B9), 20,449–20,466, https://doi.org/10.1029/96JB01925.

Vorobeva, E., J. Assink, P. J. Espy, T. Renkwitz, I. Chunchuzov, and S. P. Näsholm (2023), Probing gravity waves in the middle atmosphere using infrasound from explosions, *Journal of Geophysical Research: Atmospheres*, *128*(13), https://doi.org/https://doi.org/10.1029/2023JD038725.

Waxler, R., and J. Assink (2018), Propagation modeling through realistic atmosphere and benchmarking, in *Infrasound monitoring for atmospheric studies: Challenges in middle atmosphere dynamics and societal benefits*, pp. 509–549, Springer, https://doi.org/10.1007/978-3-319-75140-5_15.

Waxler, R., C. Hetzer, J. Assink, and D. Velea (2021), NCPAprop v2.1.0, https://doi.org/10.5281/zenodo.5562713, see also https://github.com/chetzer-ncpa/ncpaprop-release.

Waxler, R., C. H. Hetzer, J. D. Assink, and P. Blom (2022), A two-dimensional effective sound speed parabolic equation model for infrasound propagation with ground topography, *The Journal of the Acoustical Society of America*, *152*(6), 3659–3669, https://doi.org/10.1121/10.0016558.

Widemann, T., R. Ghail, C. Wilson, D. Titov, A. G. Straume, A. Ocampo, T. Bocanegra-Bahamon, L. Bruzzone, B. Campbell, L. Carter, et al. (2022), The EnVision mission to Venus, in *53rd lunar and planetary science conference*, pp. LPI–Contribution.

Zhang, J., H. Hu, and Y. Gao (2025a), Acoustic-gravity waves in a spherically layered atmosphere-solid Earth model generated by a point source on the ground, *Geophysical Journal International*, *243*(1), ggaf250, https://doi.org/10.1093/gji/ggaf250.

Zhang, S., R. Wang, X. Chen, T. Dahm, B. Xu, and Y. Zhang (2025b), Modeling Atmospheric Acoustic-Gravity Waves From Violent Volcano Eruptions With Seismological Approaches, *Journal of Geophysical Research: Solid Earth*, *130*(5), e2024JB030,911, https://doi.org/10.1029/2024JB030911.